



Published in final edited form as:

Cell. 2017 April 06; 169(2): 286–300.e16. doi:10.1016/j.cell.2017.03.020.

ESCRT-III acts downstream of MLKL to regulate necroptotic cell death and its consequences

Yi-Nan Gong¹, Cliff Guy¹, Hannes Olauson², Jan Ulrich Becker³, Mao Yang¹, Patrick Fitzgerald¹, Andreas Linkermann^{4,5,*}, and Douglas R. Green^{1,6,*}

¹Department of Immunology, St. Jude Children's Research Hospital, Memphis, TN 38105

²Division of Renal Medicine, Clinical Sciences, Intervention and Technology, Karolinska Institutet, Stockholm, Sweden

³Institute of Pathology, University Hospital of Cologne, Cologne, Germany

⁴Clinic for Nephrology and Hypertension, Christian-Albrechts-University, Kiel, Germany

⁵Division of Nephrology, Department of Internal Medicine III, University Hospital Carl Gustav Carus at the Technische Universität Dresden, Dresden, Germany

SUMMARY

The activation of Mixed Lineage Kinase-Like (MLKL) by Receptor Interacting Protein Kinase-3 (RIPK3) results in plasma membrane (PM) disruption and a form of regulated necrosis, called necroptosis. Here we show that during necroptosis, MLKL-dependent calcium (Ca⁺⁺) influx and phosphatidylserine (PS) exposure on the outer leaflet of the plasma membrane preceded loss of PM integrity. Activation of MLKL results in the generation of broken, PM “bubbles” with exposed PS that are released from the surface of the otherwise intact cell. The ESCRT-III machinery is required for formation of these bubbles, and acts to sustain survival of the cell when MLKL activation is limited or reversed. Under conditions of necroptotic cell death, ESCRT-III controls the duration of plasma membrane integrity. As a consequence of the action of ESCRT-III, cells undergoing necroptosis can express chemokines and other regulatory molecules, and promote antigenic cross-priming of CD8⁺ T cells.

Graphical abstract

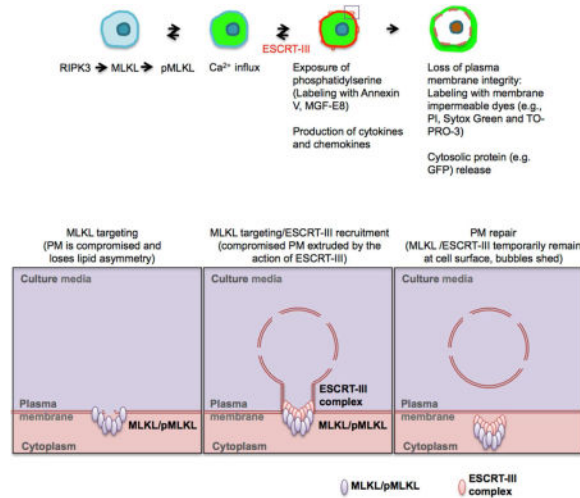
*Correspondence: douglas.green@stjude.org (D.R.G.); andreas.linkermann@uksh.de (A.L.).

⁶Lead Contact

Publisher's Disclaimer: This is a PDF file of an unedited manuscript that has been accepted for publication. As a service to our customers we are providing this early version of the manuscript. The manuscript will undergo copyediting, typesetting, and review of the resulting proof before it is published in its final citable form. Please note that during the production process errors may be discovered which could affect the content, and all legal disclaimers that apply to the journal pertain.

AUTHOR CONTRIBUTIONS

Y.G., A.L. and D.R.G. designed the experiments; Y.G., C.G., H.O., J.U.B., M.Y., P.F. and A.L. performed the experiments and analysis; and Y.G., A.L. and D.R.G. discussed results and wrote the manuscript.



INTRODUCTION

Necroptosis is a form of regulated necrosis, mediated by the action of a pseudokinase, MLKL, acting at the plasma membrane to induce membrane disruption (Zhang et al., 2016). MLKL is activated by phosphorylation of key residues within what would be the activation loop of a conventional kinase, and this is mediated by receptor-interacting kinase-3 (RIPK3). RIPK3 itself is activated by oligomerization via its RIP-homology interacting motif (RHIM), also present on TRIF (engaged by TLR signaling), the intracellular sensor DAI (engaged by DNA viruses), the interferon-induced protein kinase PKR, and RIPK1, in its active form (engaged by TNFR-family receptors, including TNFR1) (reviewed in Weinlich et al., 2017; Zhang et al., 2016). RIPK1 also regulates RIPK3 activation and necroptosis in two ways: a) in its inactive form it can prevent RIPK3 activation, even when RIPK3 is engaged independently of RIPK1, an effect that can be seen upon addition of a RIPK1 inhibitor, such as necrostatin-1s (Nec-1s) (Degeretev et al., 2013); and b) it recruits a complex of FADD, caspase-8, and c-FLIP_L, which acts as a protease to destroy the RIPK3 complex (Weinlich and Green, 2014). As a consequence, necroptosis is induced by a number of conditions, including TLR and TNFR ligation, provided FADD-caspase-8-FLIP activity is inhibited or disrupted (Vanden Berghe et al., 2016).

RIPK3 can be generated as a fusion protein with the binding domain of FKBP-12 (Fv), such that addition of a dimeric rapalog (dimerizer) triggers its activation irrespective of upstream signals. By adding two Fv regions (RIPK3-2Fv), dimerizer causes oligomerization, which can override the requirement for caspase inhibition (Orozco et al., 2014). This allows coordinated and rapid activation of RIPK3 by the addition of dimerizer alone. MLKL is similarly activated by oligomerization (Quarato et al., 2016), and therefore a fusion protein of the N-terminal region of MLKL (residues 1–181) and Fv is lethal to cells upon addition of dimerizer (Quarato et al., 2016). Both RIPK3-2Fv and human (h) MLKL^{1–181}-2Fv were employed in the studies described herein.

We found, through the use of these systems, that the activation of MLKL results in a rapid flux of Ca⁺⁺ into the cell, which was quickly followed by lipid scrambling of the plasma

membrane, such that phosphatidylserine (PS) was exposed on the cell surface prior to membrane disruption, and while PS exposure followed Ca^{++} influx, it was not dependent on Ca^{++} . Imaging of this PS exposure revealed small “bubbles” of broken plasma membrane that were released from the cell surface. We found that the formation of these bubbles depended upon the function of ESCRT-III components, and that ESCRT-III activity sustained the integrity of the plasma membrane following MLKL activation, delaying the onset of membrane permeabilization and death of the cell. As a consequence, cells dying by necroptosis have sufficient time to generate signals that affect surrounding cells. These include cytokines, chemokines, and those required for presentation of protein antigens by dendritic cells that engulf the dying cells, thereby activating CD8^+ T cells.

Further, we found that cells that exposed PS upon MLKL activation could be “resuscitated” and survive when MLKL activation was subsequently halted, and this required the function of ESCRT-III components. We also found that the influx of Ca^{++} appears to participate in this effect.

ESCRT proteins belong to several subgroups (ESCRT-I, -II, and -III) that function in endosomal trafficking, multivesicular body formation, scission of the plasma membrane, virus budding and nuclear membrane assembly during cytokinesis (Christ et al., 2017), and function in the repair of plasma membranes damaged by laser light (Jimenez et al., 2014). Our findings suggest that membrane damage caused by the activity of MLKL during necroptosis is also repaired by the function of ESCRT-III, and thus cells that harbor active MLKL can sustain survival if ESCRT is engaged.

RESULTS

Necroptotic cells expose phosphatidylserine prior to loss of plasma membrane integrity

Phosphatidylserine (PS) is localized to the inner leaflet of the plasma membrane of healthy cells by the action of lipid translocases (Leventis and Grinstein, 2010). Because of the original descriptions of PS exposure during apoptosis, this has been represented as a hallmark of apoptotic cell death, and caspase-dependent mechanisms responsible for lipid scrambling have been described (Martin et al., 1995; Segawa et al., 2014; Suzuki et al., 2013). We have found, however, that the exposure of PS prior to loss of plasma membrane integrity also occurs during necroptosis.

NIH3T3 cells expressing dimerizable RIPK3 (RIPK3-2Fv) or the N-terminal region of human MLKL (hMLKL¹⁻¹⁸¹-2Fv) rapidly undergo necroptosis when exposed to dimerizer (Orozco et al., 2014; Quarato et al., 2016). Using such cells we found that upon dimerizer (B/B) addition, cells rapidly became positive for Annexin V (AnnV) staining prior to uptake of Sytox Green (Figure 1A) or propidium iodide (PI) (Figure 1B). This effect was also observed upon addition of TNF plus the caspase inhibitor, zVAD-fmk (TZ) (Figure 1B). Silencing of MLKL prevented PS exposure upon activation of RIPK3 (Figure S1A). Similarly, ablation of MLKL (Figure S1B) prevented PS exposure in NIH 3T3 cells in response to RIPK3 oligomerization or treatment with TZ, or in HT-29 treated with TZ plus the Smac mimetic, Lcl-161 (TSZ) (Figure 1C and 1D). Therefore, the activation of MLKL causes lipid scrambling to expose PS. Consistent with these results, MFG-E8, another PS-

binding protein, also labeled cells undergoing necroptosis (Figure 1C and 1D). This effect, unlike that observed during apoptosis, was not inhibited by caspase inhibitors (Figure S1C). Further, PS exposure during necroptosis was observed in cells lacking TMEM16F (Figure S1D), necessary for PS exposure in response to Ca^{++} influx (Suzuki et al., 2010). Similarly, PS exposure during necroptosis was observed in the absence of extracellular Ca^{++} , as measured by MFG-E8 staining, which does not require Ca^{++} for binding to PS (Dasgupta et al., 2006) (Figure S1E).

To visualize AnnV binding to cells undergoing necroptosis, z-stacked images were collected over time in cells expressing cytosolic mCherry. Strikingly, upon addition of B/B to 3T3 cells expressing RIPK3-2Fv or hMLKL¹⁻¹⁸¹-2Fv, we observed a rapid generation of small (approx. 0.5 μm) AnnV⁺ “bubbles” that formed at the plasma membrane (Figure 1E, Movies S1). Similar AnnV⁺ bubbles were observed in mouse embryonic fibroblasts, (MEF, Figure S1F) and HT-29 (Figure S1G) cells treated with TSZ. It is noteworthy that the NIH 3T3 cells employed in these experiments lack endogenous RIPK3 (Figure S2A), and MLKL¹⁻¹⁸¹ does not bind RIPK3 (Xie et al., 2013). Thus, the formation of bubbles upon oligomerization of MLKL¹⁻¹⁸¹ (Figure 1E, Movie S1) may be a direct consequence of active MLKL.

The formation of plasma membrane bubbles upon RIPK3 activation was also observed by labeling the plasma membrane with DiIC₁₈(3) (DiI) (Figure S2B). We found that MLKL was required for formation of these bubbles in response to RIPK3 oligomerization or treatment with TZ (Figure 2A and S2C).

A minimum fragment of MLKL capable of causing plasma membrane disruption when dimerized, MLKL¹⁻¹⁴⁰, translocates and associates with the plasma membrane upon activation (Quarato et al., 2016). We utilized cells expressing MLKL¹⁻¹⁴⁰-2Fv-Venus to visualize the relationship between active MLKL and the generation of plasma membrane bubbles. Upon addition of B/B, MLKL¹⁻¹⁴⁰-2Fv associated with the plasma membrane (Figure 2B). Strikingly, AnnV⁺ bubbles formed after MLKL membrane targeting and at sites at which MLKL accumulated at the membrane (Figure 2B and 2C). Taken together, these observations suggest that active MLKL functions to induce the formation of the plasma membrane bubbles.

Unlike apoptotic bodies, these MLKL-induced bubbles appeared to be largely devoid of cytosolic content, as evidenced by the absence of cytosolic mCherry (Figure 1E, movies S1), which we confirmed by electron microscopy (Figure 2D). Further, the bubbles were permeable to 10kDa dextran-NH₂ (Figure 2E). These observations are consistent with the idea that the bubbles are comprised of broken membranes that are shed from the cell surface.

ESCRT-III is responsible for formation of MLKL-induced AnnV⁺ bubbles

Active MLKL causes plasma membrane damage (Zhang et al., 2016). Although plasma membrane damage repair is generally not associated with the formation and shedding of membrane bubbles (Andrews et al., 2014), plasma membranes that are damaged by laser light can extrude broken membrane, a process that is dependent on the ESCRT-III complex components CHMP4B and VPS4 (Jimenez et al., 2014). We therefore asked whether the formation of bubbles induced by active MLKL is a function of ESCRT-III.

NIH3T3 cells expressing RIPK3-2Fv or hMLKL¹⁻¹⁸¹-2Fv were transiently transduced with GFP-CHMP4B and imaged following the addition of B/B. Strikingly, CHMP4B rapidly translocated to the plasma membrane upon activation of either RIPK3 or MLKL (Figure 3A, Movie S2) or upon treatment with TSZ (Figure S3A, Movie S2). After translocation, CHMP4B co-localized with MLKL in puncta at the plasma membrane (Figure 3B), and at sites at which AnnV⁺ bubbles formed (Figure 3C and D, Movie S2). Further, this translocation of CHMP4B was dependent on MLKL, as it did not occur upon RIPK3 activation in *mlkl*^{-/-} cells (Figure 3E and S3B, Movie S2).

We noted that in cells that underwent plasma membrane permeabilization, the puncta containing co-localized MLKL and CHMP4B remained associated with the membrane, while the cytosolic proteins were released (movie S2). We therefore used flow cytometry to assess the persistence of these proteins following digitonin treatment of cells in which CHMP4B-mCherry was stably expressed (Figure S3C) and MLKL was activated. We observed that both MLKL¹⁻¹⁴⁰-2Fv-Venus and CHMP4B-mCherry sustained digitonin-resistant fluorescence following addition of B/B (Figure S3D). Therefore, active MLKL induces CHMP4B translocation to the PM. Similarly, CHMP4B-mCherry fluorescence was sustained in digitonin-treated cells in which RIPK3 had been activated and MLKL was present (Figure S3E).

Using this system, we examined several ESCRT components for their potential roles in CHMP4B-mCherry stabilization following addition of B/B to cells expressing MLKL¹⁻¹⁴⁰-Venus-2Fv, as an indication of CHMP4B translocation. Of those tested, silencing of the ESCRT-I component TSG101 prevented CHMP4B translocation following MLKL activation (Figure 3F). Silencing of TSG101 had no effect on the sustained fluorescence by FACS (Figure 3F) and plasma membrane localization (Figure S3F and S3G) of MLKL¹⁻¹⁴⁰-Venus-2Fv following addition of B/B, but prevented translocation of CHMP4B-mCherry to the plasma membrane (Figure S3F and S3G).

To determine if ESCRT-III functions in the formation of AnnV⁺ bubbles following MLKL activation, we silenced the ESCRT-III components CHMP2A and CHMP4B. We found that the formation of plasma membrane bubbles following activation of RIPK3 or MLKL was dependent on the presence of these ESCRT-III components (Figures 3G-I, S4A). Similarly, silencing of CHMP2A reduced the formation of AnnV⁺ bubbles observed when HT-29 cells were treated with TSZ (Figure S4B and S4C).

During necroptosis, an influx of Ca⁺⁺ has been described, although its role in necroptosis is controversial (Cai et al, 2014, Wang et al, 2014a). Using the Ca⁺⁺ sensor GCaMP3, we confirmed that an influx of Ca⁺⁺ occurred following activation of MLKL, preceded the exposure of PS (Figure S4D, Movie S3), and was dependent on the presence of MLKL (Figure S4E-G). Therefore, intracellular Ca⁺⁺ is elevated upon MLKL activation (independently of RIPK3), prior to the recruitment of ESCRT-III for the formation of AnnV⁺ bubbles. Although Ca⁺⁺ was not required for PS exposure (Figures S1D and S1E), we found that extracellular Ca⁺⁺ was required for the translocation of CHMP4B (Figure S4H and S4I), and for the formation of plasma membrane bubbles (Figure S4I).

ESCRT-III antagonizes necroptosis

ESCRT-III is required for cell viability, which is often ascribed to its roles in endosomal trafficking and mitosis (Christ et al., 2017). Indeed, we found that silencing of CHMP2A in NIH 3T3 cells induced approximately 20% cell death (Figure 4A and B) that was blocked by expression of human CHMP2A, which is resistant to silencing of the murine CHMP2A (Figure 4A), and not affected by the caspase inhibitors qVD-oph and z-VAD (Figure S5A), suggesting that the death was non-apoptotic. Silencing of either RIPK3 or MLKL prevented this cell death (Figure 4B and S4A). Similarly, silencing of CHMP4B in L929 cells caused extensive cell death (Figure 4C), and this was prevented by silencing of RIPK3 or MLKL (Figure 4D and S5B), addition of the RIPK1 inhibitor Nec-1s or ablation of MLKL (Figure 4E and 4F). Therefore, silencing of ESCRT-III in these cells induced necroptosis. The spontaneous necroptosis in L929 cells upon silencing of CHMP4B was prevented by antibody neutralization of autocrine TNF (Figure 4G and S5C).

Silencing of human CHMP2A in HT-29 cells sensitized cells to necroptosis induced by sub-optimal concentrations of TSZ (Figure S5D) and permitted the induction of cell death upon addition of TNF plus z-VAD, without a need for Smac mimetic (Figure S5E). This cell death, inhibited by either Nec-1s or the MLKL inhibitor, necrosulfonimide (NSA) (Sun, et al. 2012), as well as MLKL ablation, was therefore likely to be necroptosis (Figure S5E and S5F). We also observed the same effect with TSG101 silencing (Figure S5G and S5H). We did not examine the role of CHMP4B in HT-29 cells, as unlike murine cells, human cells express an additional CHMP4A protein.

Silencing ESCRT components, including the ESCRT-III components CHMP4B, VPS4B (Figure 4H, 4I) or CHMP2A (Figure S6A) or the ESCRT-I components TSG101 or VPS37B, sensitized murine cells to the induction of cell death upon addition of TNF alone (Figure 4H and 4I), which was blocked by addition of the RIPK1 inhibitor Nec-1s (Figure 4J) or silencing RIPK3 (Figure S6A). Addition of z-VAD to ESCRT-silenced murine L929 cells induced more rapid necroptosis than that induced in control cells treated with scrambled siRNA (Figure 4K). Silencing of another ESCRT-III component, IST1, also showed a similar but milder effect to accelerate necroptosis (Figure S6B). Importantly, the sensitization for cell death under conditions of necroptosis in cells in which ESCRT was silenced was not observed under conditions promoting apoptosis (Figure 4L and S6C). This suggests that the enhanced response to TNF or TZ is not due to changes in TNF signaling in ESCRT silenced cells, but rather due to a change in susceptibility to the effects of active MLKL. This was further supported by the finding that cells sensitized by silencing of CHMP2A to induction of cell death upon TNF addition (Figure S6A) displayed the same I κ B α degradation (Figure S6D) and MLKL phosphorylation (Figure S6E) as did cells treated with scrambled siRNA. This lack of change in TNFR signaling was also observed for cells silenced for VPS37B and TSG101 (Figure S6F). Intriguingly, we also observed no elevation in detectable phospho-MLKL upon addition of TNF alone, despite extensive MLKL dependent cell death (Figure S6A and S6E). This is in contrast to the readily detectable levels of phospho-MLKL in ESCRT-silenced cells that were treated with TZ (Figure S6E). This suggests that the caspase-8-dependent inhibition of MLKL (Vanden Berghe et al., 2016; Weinlich et al., 2017) serves to restrict phospho-MLKL to undetectable

levels, which are nevertheless sufficient to engage MLKL-dependent death of the cells when ESCRT-III activity is compromised.

To further test this idea, we examined WT and MLKL-deficient L929 cells in response to TNF, with or without interferon- β (IFN β), which induces increased MLKL expression (Figure S6G). Remarkably, we observed that treatment with TNF alone induced the formation of AnnV⁺ bubbles that was enhanced by IFN β , but did not occur in the absence of MLKL (Figure S6H). This suggests that TNF induces sufficient activation of MLKL to engage ESCRT-III-mediated bubble formation, which prevents the MLKL-dependent cell death unless ESCRT-III is compromised.

Quantification of the timespan between the earliest MLKL-dependent event following treatment with B/B (Ca⁺⁺ influx, as indicated by GCaMP3 fluorescence) and the loss of plasma membrane integrity revealed that silencing of either CHMP2A or CHMP4B greatly reduced the time required for active MLKL to disrupt plasma membrane integrity (Figure 4M).

Taken together, our results show that ESCRT-III functions to prevent or delay the loss of plasma membrane integrity caused by active MLKL. We suggest that this is due to active repair of plasma membranes damaged by MLKL, which manifests as the broken AnnV⁺ bubbles we observed. When MLKL-dependent cell death occurs, we suggest that this repair is pyrrhic, ultimately overcome by the action of MLKL. This raises the question of what function a delay in necroptosis might have, addressed next.

ESCRT-III activity allows necroptotic cells to generate and release signaling molecules

Conditions that promote necroptosis, including TNFR and TLR ligation, also induce expression of inflammatory cytokines. Further, engagement of RIPK1 (Yatim et al., 2015) or activation of MLKL (Kang et al., 2015; Kang et al., 2013; Lawlor et al., 2015; Wang et al., 2014b), promotes NF- κ B activation and inflammasome activation, respectively. Indeed, such observations raise the question of whether it is the activation of the pathway, or necroptosis itself, that promotes inflammation *in vivo* (Wallach et al., 2016).

We examined the transcriptional profile of AnnV⁺, Sytox Green⁻ NIH3T3 cells following activation of hMLKL¹⁻¹⁸¹-2Fv. Among the transcripts induced by active MLKL (in the absence of other signals, e.g. RIPK3, which is not expressed in NIH3T3 cells), the chemokines CXCL10 and CXCL1 were the most prominent (Figure 5A, Table S1). We therefore reasoned that once MLKL is activated, cells must remain alive for a sufficient period of time to permit the production of signals such as chemokines, which suggested that the ESCRT-III-mediated delay in cell death sustains cells to allow such signaling. To test this, we examined CXCL10 and CXCL1 protein production following hMLKL¹⁻¹⁸¹-2Fv in cells with or without CHMP2A or CHMP4B. We found that cells lacking ESCRT-III function produced less of these chemokines than did control cells (Figure 5B and 5C).

RIPK3 can promote the production of inflammatory cytokines (Wallach et al., 2016). Activation of RIPK3-2Fv in immortalized macrophages (iMacs) induced cell death that was accelerated by the silencing of CHMP2A (Figure 5D and 5E). Upon RIPK3 activation by

B/B, these cells produced a variety of cytokines and chemokines (Figure 5F). Strikingly, silencing of CHMP2A reduced such cytokine production, presumably due to the acceleration of necroptosis. This was supported by the finding that the production of cytokine in response to LPS was not affected by silencing of CHMP2A (Figure 5G). Therefore, ESCRT-III functions to delay or prevent cell death caused by MLKL sufficiently to allow signals such as cytokines and chemokines to manifest prior to the demise of the cell.

Cross-priming, a process critically involved in CD8⁺-dependent anti-viral and anti-tumor responses, occurs when a dendritic cell engulfs a dying cell and presents associated antigenic peptides on its own class I MHC molecules (Albert et al., 1998). Necroptotic cells are potent inducers of cross-priming, but the process requires the engagement of NF- κ B signaling by RIPK1 (Yatim et al., 2015). This suggests that for cross-priming to occur following the induction of necroptosis, a sufficient time delay is necessary to allow for NF- κ B-dependent production of the requisite mediators. To test this idea, CHMP2A was silenced in RIPK3-2Fv-NIH3T3 cells expressing membrane-bound ovalbumin (OVA) (Yatim et al., 2015), before treatment with B/B and injection into C57Bl/6 mice. Cross-priming of CD8⁺ T cells was then assessed by binding of a pentamer of H-2K^b bearing the OVA peptide, SIINFEKL. While B/B-treated cells induced increased numbers of OVA-specific T cells, silencing of CHMP2A significantly dampened the induction of cross-priming by the dying cells (Figure 5H and I). Therefore, the ESCRT-III-mediated delay in the timing of cell death upon activation of RIPK3 is important to promote cross-priming.

These results, taken together, suggest that the regulation of the timing of necroptosis by ESCRT-III has physiological significance as it allows the cell, as it dies, to signal surrounding cells.

Active MLKL is not a “point-of-no-return” for cell survival

MLKL activation is necessary and sufficient for Ca⁺⁺ flux, PS exposure, recruitment of ESCRT-III activity, and the death of the cell. We therefore asked at what point active MLKL commits a cell to death, and whether ESCRT-III counters this commitment. In other words, we asked if cells with active MLKL that have not lost plasma membrane integrity are nevertheless committed to death, or are alive. To address this we took advantage of our observation that PS exposure, induced by active MLKL, can be detected by the binding of AnnV and sorted on this basis.

We activated RIPK3-2Fv in cells by addition of B/B and sorted AnnV⁺, Sytox Green⁻ cells (Figure 6A). We then returned the cells to culture and added the monomeric form of the Fv-binding agent, termed “washout,” which competes with B/B dimers and disrupts oligomers induced by its presence. When AnnV⁺, Sytox Green⁻ cells were cultured without washout agent, they progressed to AnnV⁺, Sytox Green⁺ cells, as expected. Strikingly, however, addition of the washout agent to these AnnV⁺ cells resulted in the appearance of a population of AnnV⁻, Sytox Green⁻ cells (Figure 6B and 6C), suggesting that the AnnV⁺ cells had been “resuscitated” to maintain their survival. To further confirm this, we cultured sorted, AnnV⁺, Sytox Green⁻ cells following RIPK3-2Fv activation with or without the washout agent. AnnV⁺ cells without washout did not expand in culture, while those with

addition of washout showed robust growth (Figure 6D). Time lapse images revealed rounded, non-adherent cells that attached and regained normal morphology when the washout agent was added (Figure 6E). Similarly, using the Ca^{++} -reporter GCaMP3, we found that the elevated Ca^{++} levels rapidly decreased to resting levels when washout agent was present (Figure S7A and S7B). While AnnV^+ , Sytox Green $^-$ cells following RIPK3-2Fv activation harbored phospho-MLKL (Figure 6F), as expected (Sun et al., 2012; Wang et al., 2014a), the washout treatment-derived AnnV^- , Sytox Green $^-$ cells did not have detectable phospho-MLKL. The inability to detect MLKL in the bubbles shed during necroptosis (as neither MLKL $^{1-140}$ nor MLKL $^{\text{FL}}$ is detected in the bubbles in Figure 2B and S1F), and the failure to prevent cellular resuscitation by inhibition of the proteasome (Figure S7C) may reflect the removal of phosphate groups from the activation loop of MLKL via the activity of a phosphatase, yet to be identified. Consistent with this hypothesis, cells expressing N-terminal FLAG-tagged MLKL (which lacks necroptotic activity but can be phosphorylated by RIPK3, Figure S7D and S7E) were also able to remove the phosphate from phospho-MLKL after the addition of the washout agents. This dephosphorylation was not prevented by inhibition of either proteasome activity or lysosomal degradation (Figure S7E). The recovered NIH3T3 cells showed no difference from previously untreated (parental) cells in their response to B/B (Figure 6G), and thus, resuscitation did not select for a subpopulation of cells resistant to cell death. The same resuscitation also occurred in RIPK3-2Fv-expressing iMac (Figure 6H, 6I and S7F). These findings indicate that cells harboring active MLKL remain alive and can be resuscitated if the signaling responsible for MLKL activation is disrupted.

NSA is an inhibitor of human, but not mouse, MLKL (Sun et al., 2012). Murine 3T3 cells expressing RIPK3-2Fv or hMLKL $^{1-181}$ -2Fv were treated with B/B, sorted for AnnV^+ , Sytox Green $^-$ cells, and returned to culture with washout agent or NSA. As in our previous experiments, the addition of washout promoted the appearance of AnnV^- , Sytox Green $^-$ cells (resuscitation). Addition of NSA to the cells expressing hMLKL $^{1-181}$ -2Fv similarly promoted resuscitation, while it had no effect in the cells expressing RIPK3-2Fv (Figure S7G and S7H), since the latter relies on murine MLKL for necroptotic effects and NSA had no effect on the function of the active murine MLKL. Time-lapse imaging of B/B-treated hMLKL $^{1-181}$ -2Fv cells recultured in washout or NSA showed rounded cells attaching and assuming a normal morphology and thus, resuscitation (Figure S7I). Therefore, inhibition of active MLKL by NSA can permit resuscitation of AnnV^+ , Sytox Green $^-$ cells.

This allowed us to examine resuscitation in cells responding to more conventional inducers of necroptosis. HT-29 cells were treated with TSZ and sorted for AnnV^+ , Sytox Green $^-$ cells, which were then returned to culture with NSA (Figure 6J and 6K). Culture of the TSZ-treated AnnV^+ , Sytox Green $^-$ HT-29 cells showed that NSA promoted cell survival and growth of these cells (Figure 6L). Phospho-MLKL was present in TSZ-treated AnnV^+ , Sytox Green $^-$ HT-29 cells, but following treatment with NSA, the levels of phospho-MLKL declined (Figure 6M). The recovered HT-29 cells, when expanded and re-treated, showed no difference from parental cells in their response to TSZ (Figure 6N), and therefore resuscitation does not represent a selection for a subpopulation of cells resistant to cell death. Similar resuscitation results were obtained with TSZ-treated Jurkat cells (Figure S7J and S7K).

ESCRT components are necessary for resuscitation of cells with active MLKL

Our data indicate that upon activation of MLKL, cells become AnnV⁺, and sustain their survival at least temporarily, such that disruption of the signals responsible for activation of MLKL allows the cells to become AnnV⁻ and sustain viability. Because we had found that ESCRT components antagonizes the effects of active MLKL, it followed that these components are also necessary for preserving survival of AnnV⁺ cells with active MLKL.

We therefore silenced CHMP2A or CHMP4B in NIH3T3 cells expressing RIPK3-2Fv or hMLKL¹⁻¹⁸¹-2Fv, treated with B/B, and sorted AnnV⁺, Sytox Green⁻ cells. Cells were returned to culture with washout agent, and substantial numbers of AnnV⁻, Sytox Green⁻ cells appeared. This resuscitation effect was dramatically reduced in cells in which the ESCRT-III components, CHMP2A or CHMP4B, were silenced (Figure 7A and B). Enforced expression of human CHMP2A, resistant to the siRNA for murine CHMP2A, partially blocked the inhibitory effects of silencing murine CHMP2A on resuscitation (Figure S8A). Silencing human CHMP2A in HT-29 cells similarly impacted resuscitation of TSZ-treated AnnV⁺, Sytox Green⁻ cells by NSA (Figure 7C).

We then employed the resuscitation assay to survey components of the ESCRT pathway involved in the preservation of AnnV⁺, Sytox Green⁻ cells. In addition to CHMP2A and CHMP4B, other ESCRT-III components appeared to function in sustaining cells for resuscitation, including CHMP3, CHMP7, IST1, as well as the ATPase complex proteins, VPS4A and VPS4B, involved in recycling of CHMP4 (Carlton, 2010) (Figure 7D). We were unable, however, to identify roles for the ESCRT-III components CHMP1A, CHMP1B, CHMP2B, or CHMP6 (Figure 7D and S8D). We also found roles for the ESCRT-0 component, HGS/HRS, and the ESCRT-I components TSG101 and VPS37B. In contrast, we were unable to find roles for the accessory components ALG2, PTPN23, or ALIX. All the siRNA silencing effects were verified by qRT-PCR or immunoblot (Figure S8B and S8C), although negative results of such silencing cannot be taken as evidence that these components are not involved. Our results show that components of the ESCRT machinery are involved in sustaining cells with active MLKL, thereby allowing resuscitation of living cells from the AnnV⁺ pool, provided that signaling for necroptosis is disrupted. Similarly, Ca⁺⁺ influx, required for light-damage repair (Jimenez et al., 2014; Scheffer et al., 2014), also appeared to function in resuscitation. Treatment of cells with the Ca⁺⁺-chelator, BAPTA-AM, prevented the appearance of AnnV⁻, Sytox Green⁻ cells when RIPK3-2Fv or MLKL signaling was disrupted by addition of the washout agent (Figure S8E).

To further explore the resuscitation phenomenon, we treated NIH 3T3 cells expressing RIPK3-2Fv with B/B and sorted AnnV⁺ SytoxGreen⁻ cells, which were then briefly treated with washout and injected into mice, where they formed tumors to approximately the same extent as did untreated cells (Figure 7E). While transiently silencing CHMP2A had no significant effect on the ability of the otherwise untreated cells to form tumors, it significantly decreased tumor formation in the resuscitated cells.

Our findings suggest that cells can sustain a level of active, phospho-MLKL, provided that some components of the ESCRT machinery are active. Therefore, conditions should exist under which this effect results in cell survival despite MLKL activation. We identified a

clone of iMac cells expressing RIPK3-2Fv that showed minimal cell death upon treatment with B/B (Figure 7F, this clone, noted as RIPK3-2Fv-iMac*, is different from that used in Figure 5D and 5E). Remarkably, we observed that treatment with B/B induced extensive formation of AnnV⁺ bubbles (Figure S8F and S8G), which suggests that ESCRT-III-mediated bubble shedding is able to prevent cell death in this clone. Consequently, silencing of CHMP2A in these cells resulted in dramatically increased susceptibility to necroptosis upon RIPK3 activation. As a consequence, B/B treatment did not prevent long term survival and expansion of the cells unless CHMP2A was silenced (Figure 7G). Despite this, disruption of ESCRT in these cells had no effect on the levels of phospho-MLKL induced by RIPK3 activation (Figure 7H). Therefore, ESCRT-III activity can limit the ability of phospho-MLKL to kill cells, consistent with our other observations.

We therefore sought evidence that this can occur in stressed tissues *in vivo*. Healthy human kidney tissue, obtained from living donor biopsies immediately after excision for transplantation was stained for phospho-MLKL (Figure 7I and 7J). At this time point, the samples did not exhibit any positive signal for phospho-MLKL. In contrast, during the process of transplantation into the recipient, pronounced phospho-MLKL positivity developed in endothelial cells as detected in a second biopsy sample obtained within one hour after the transplantation process from the same kidneys now in recipient (Figure 7I and 7J). Importantly, these stressed cells appeared normal without any signs of cell death in all samples investigated (Figure 7I).

RNAseq analysis of biopsied tissue pre- versus post-transplant showed an elevation of RIPK1 and MLKL, as well as several components of the ESCRT machinery involved in the resuscitation of murine cells, including HGS, VPS37B, IST1, VPS4A and CHMP4B (Figure 7K, Supplemental Table S2). Consistent with this, we interrogated a public database of expression data of murine kidney tissues following ischemia-reperfusion injury (Liu et al., 2014) (Figure S8H, Supplemental Table S2). Again, expression of several ESCRT components was elevated, especially in nephrons, endothelium, and macrophages. It is therefore possible that ESCRT function can sustain tissues that are otherwise susceptible to necroptosis upon stress. If so, cells with elevated expression of ESCRT components may survive preferentially. To test this idea, we returned to our resuscitation system and compared mRNA expression in MLKL-induced AnnV⁺, SytoxGreen⁻ cells before and after resuscitation with the washout agent. The cells that survived this treatment displayed elevated levels of expression of a number of ESCRT components (Figure S8I), consistent with the idea that we had selected for cells with such elevated expression. While it is unclear how stress, such as ischemia-reperfusion injury induces expression of ESCRT components, those cells with such elevated expression appear to be more resistant to the necroptotic effects of RIPK3-induced MLKL activation.

DISCUSSION

When a cell undergoes apoptosis, PS is no longer restricted to the inner leaflet of the plasma membrane, owing to the caspase-dependent activation of a phospholipid scramblase and the inactivation of a phospholipid flippase (Segawa et al., 2014; Suzuki et al., 2013). Thus, AnnV labeling is widely used as a hallmark to label dying cells as “apoptotic” (Leventis and

Grinstein, 2010; Martin et al., 1995). However, we found that necroptotic cells can be stained with either AnnV or MFG-E8 prior to disruption of plasma membrane integrity, suggesting that cells undergoing necroptosis also scramble PS to the out leaflet of the plasma membrane. Three mechanisms have been described for phospholipid scrambling leading to PS exposure: Ca^{++} -mediated activation of TMEM16F (Suzuki et al., 2010), caspase-mediated activation of Xkr8 (Suzuki et al., 2013) and caspase-mediated inactivation of the “flippase” complex, ATP11c and CDC50a (Segawa et al., 2014). We have found, however, that PS exposure during necroptosis proceeds independently of TMEM16F or Ca^{++} , and independently of caspases. Further, PS externalization occurs within 5 min of RIPK3 and MLKL activation, making it unlikely that the effect is due to inactivation of translocases necessary for “flipping” PS to the inner leaflet. Given the direct association of active MLKL with the plasma membrane (Zhang et al., 2016), it is possible MLKL itself may directly cause the scrambling of the plasma membrane to expose PS.

When ESCRT-III is functional and MLKL is active, membranes with exposed PS are rapidly shed as apparently broken “bubbles” (Figure 1E). In contrast, when ESCRT function is disrupted, PS exposure upon MLKL activation manifests evenly, throughout the plasma membrane, and cells die more rapidly than when ESCRT is active. This is not due to cells with disrupted ESCRT function being “unhealthy” because while those cells died more rapidly by necroptosis, their apoptotic death was not affected (Figure 4K and 4L). Intriguingly, disruption of ESCRT also sensitized some cells for the induction of necroptosis by TNF, without the usual requirement to inhibit caspase activity. This suggests that the action of a low level of MLKL activation by engagement of TNFR that escapes control by the action of FADD-caspase-8-FLIP (Dillon et al., 2012; Kaiser et al., 2011; Oberst et al., 2011) is normally suppressed by the repair function of ESCRT-III, such that cells survive. This was supported by our observation that TNF induced MLKL-dependent AnnV⁺ bubbles in cells with intact ESCRT-III activity (Figure S6H). The alternative explanation, that disruption of ESCRT-III alters TNFR signaling to promote necroptosis, is unlikely, as TNF-induced $\text{I}\kappa\text{B}\alpha$ degradation or apoptosis induced by TNF plus CHX were unaffected when ESCRT-III components were silenced, and no differences in the levels of TNF-induced phospho-MLKL were detected (Figure S6C to S6F). This is consistent with a report (Maminska et al., 2016) that although ESCRT-III functions to suppress spontaneous NF- κB activation in 293 cells as a consequence of intracellular TNFR accumulation and signaling, ESCRT-III does not affect NF- κB activation by extracellular TNF addition. While another report (Mahul-Mellier et al., 2008) suggested that the ESCRT components Alix and ALG-2 promote caspase-8 activity and apoptosis upon treatment with TNF, we were unable to find a role for these ESCRT components in necroptosis. Secondly, although the induction of necroptosis by TNF in cells in which ESCRT-III was disrupted was dependent on RIPK3 and MLKL and suppressed by the RIPK1 inhibitor, Nec-1s, we observed no detectable increase in phospho-MLKL, such as that observed upon treatment with TNF plus caspase-inhibitor (Figure S6E). Thus, silencing of ESCRT-III did not alter the level of activated phospho-MLKL upon TNF treatment, but altered the response of the cell such that necroptosis ensued in an MLKL-dependent manner.

Upon induction of necroptosis, many cells may eventually die, despite the activity of ESCRT-III. This does not appear to be due to suppression of ESCRT-III, but rather a simple

“over-whelming” of the repair function. This is apparent in time-lapse images (see Supplemental Movie S1), where the formation of ESCRT-dependent bubbles continues up to the moment that plasma membrane integrity is lost.

During apoptosis, PS exposure may represent a “point of no return”. In contrast, PS exposure during necroptosis is dependent on MLKL, and does not represent an inevitable lethality for the cell; disruption of RIPK3 or MLKL function in Annexin V⁺ cells allows a substantial percentage of cells to be resuscitated, and capable of clonal growth. We observed this resuscitation in several cell lines, both human and mouse, including NIH3T3, MEF, Jurkat, immortalized macrophages and HT-29 cells. These data suggest that the function of ESCRT to inhibit necroptosis represents a general feature of this form of cell death. In general, we noticed that resuscitation following disruption of RIPK3 activation was less effective than that seen when active MLKL was disrupted, probably due to the continued presence of phospho-MLKL in the former. Those cells that were resuscitated following disruption of RIPK3 activity showed a loss of phospho-MLKL, possibly by the action of a yet undefined phosphatase.

In addition to the ESCRT-III components CHMP2A, CHMP4B, and the VPS4 proteins involved in CHMP4B disassembly, we identified several other ESCRT components that showed effects on resuscitation, sensitivity to TNF or TZ, and/or the kinetics of necroptotic cell death (summarized in Supplemental Table S3). While one of these, the ESCRT-I component TSG101, was demonstrably required for translocation of CHMP4B to the plasma membrane upon MLKL activation, the precise roles for other components in sustaining survival of cells with active MLKL are not clear. Importantly, however, while ESCRT has a number of functions that are important for long-term cell viability, the lethal effects of transiently silencing ESCRT in our systems (leading to either spontaneous or TNF-induced death) was consistently prevented by blockade of necroptosis by Nec-1s, or co-silencing of RIPK3 or MLKL. Therefore, at least in the short term, a major function for ESCRT is protection from necroptosis.

The ability of cells to survive despite active MLKL was dependent on elevated Ca⁺⁺ and several ESCRT components, some of which have also been implicated in the repair of light-damaged plasma membranes (Jimenez et al., 2014). Plasma membrane repair is often initiated by an influx of Ca⁺⁺ (Jimenez et al., 2014; Scheffer et al., 2014). In the repair of light-induced membrane damage, ESCRT-III appears to be promoted by the interaction of Ca⁺⁺ with the ESCRT accessory components Alix and Alg-2 (Scheffer et al., 2014). While Ca⁺⁺ appears to also be important to engage ESCRT-III-dependent membrane repair following MLKL activation, we were unable to identify roles for these proteins in this process. Instead, we found that other ESCRT components that engage CHMP2 and CHMP4 may function in this regard, including TSG101 and possibly IST1. Intriguingly, IST1 has been reported to function with CHMP1B in membrane abscission (McCullough et al., 2015), although we failed to identify a role for CHMP1B in survival of cells with active MLKL. This suggests that either our silencing strategy was insufficient to elucidate the role of these ESCRT components in the response to MLKL-induced membrane damage, or this process may be distinct from that of other ESCRT functions.

MLKL contains a nuclear localization sequence in its C-terminal region. During necroptosis, active MLKL translocates to the nucleus (Yoon et al., 2016), where it might influence transcription. MLKL activation also leads to Ca^{++} influx, which can also impact transcription (Figure S4D). Thus, it is possible that some transcriptional events may represent a signature of cells undergoing necroptosis. Indeed, we found that the oligomerization of the N-terminal region of MLKL was sufficient to trigger the transcription of several chemokines and immunoregulatory molecules (Supplemental Table S1).

Unlike apoptosis, necroptosis is an “immunogenic” cell death. In our *in vitro* experiments, ESCRT-III delayed cell death dynamics to maximize inflammatory cytokine production (Figure 5B–F). During necroptosis, RIPK1-induced NF- κ B was found to be required for efficient CD8⁺ T cross-priming (Yatim et al., 2015). Consistent with our *in vitro* findings, ESCRT-III was required for optimal cross-priming of CD8⁺ T cells by necroptotic cells *in vivo* (Figure 5H and 5I). It is also possible that ESCRT-III may regulate the consequence of necroptosis via the generation of bubbles released from the dying cells. The release of ESCRT-III mediated extracellular vesicles can engage the Hedgehog pathway and T cell receptor activation in other settings (Choudhuri et al., 2014; Matusek et al., 2014), and it is therefore possible that necroptotic cells may similarly recruit their neighboring cells to initiate a response by the release of membrane bubbles. However, we were unable to isolate these bubbles (due to contamination with cellular debris), nor could we identify cytosolic protein (soluble mCherry) within them.

ESCRT-III functions in the repair of light-induced plasma membrane damage (Jimenez et al., 2014; Scheffer et al., 2014), multivesicular body formation, virus budding and cytokinesis abscission (Christ et al., 2017). Other functions include nuclear envelop reassembly in mitosis, clearance of defective assembly intermediates of the nuclear envelop pore complex, neuron pruning, and nuclear envelop rupture repair during cell migration (Christ et al., 2017). Here we show that ESCRT-III is also necessary for shedding of plasma membrane that has been damaged during necroptosis, thus preserving the survival of cells in which MLKL has been activated. This effect permits cells undergoing necroptosis to express proteins with functions in surrounding cells, including the process of antigen cross-presentation upon engulfment of the dying cell.

STAR METHODS

CONTACT FOR REAGENT AND RESOURCE SHARING

As Lead Contact, Douglas R. Green is responsible for all reagent and resource requests. All requests for non-commercial reagents will be fulfilled. Please contact Douglas R. Green (douglas.green@stjude.org) with requests and inquiries.

EXPERIMENTAL MODEL AND SUBJECT DETAILS

Compounds, antibodies and reagents—The dimerizer (B/B) and its competitor (washout) were purchased from Clontech. The cytokines used were: mTNF α (Peprotech), mIFN β (PBL Assay Science) and hTNF α (Peprotech). The SMAC mimetic and inhibitor of IAP (LCL-161) was purchased from Chemietek. Other reagents included CHX (C7698,

sigma), Q-VD-OPh (qVD, A8165, Apexbio), 7-Cl-O-Nec-1 (Nec-1s, 504297, calbiochem), zVAD-fmk (A1902, Apexbio), MG132 (Sigma), Necrosulfonamide (NSA, calbiochem), LPS (Sigma), BAPTA-AM (Tocris) and Bafilomycin A1 (Sigma). Antibodies used for immunoblotting in this study were anti-actin (sc-1616, Santa Cruz) anti-FLAG (A8592, Sigma), anti-HA (H6908, Sigma), anti-hMLKL (M6697, Sigma), anti-mMLKL (AP14272b, Agent), anti-pMLKL (ab187091, Abcam), anti-RIPK3 (NBP1-77299, Novus), anti-ALIX (3A9, 2171S, Cell signaling Technology), anti-CHMP2B (ab33174, abcam), anti-CHMP4B (ab105767, abcam), anti-TSG101 (4A10, ab83, abcam) anti-TNF (Clone XT3.11 from BioXCell) and anti-I κ B α (C-21, Santa Cruz).

Plasmids—Flag-hCHMP2A, “humanized” mMLKL-HA, full-length and truncated hMLKL with two Fv domains and HA tag were cloned into pMX-IRES-mCherry. Flag-MLKL was cloned into pMX-IRES-GFP. mMLKL-mCherry and hCHMP4B-mCherry was cloned into pBabe-puro. GCaMP3 was cloned into pLZRS vector. GFP-CHMP4B expressing plasmid was a gift from Dr. Paul Bieniasz (Rockefeller University). Tfr-OVA expressing plasmid was a gift from Dr. Helen Beere (St. Jude Children’s Research Hospital). The hCHMP4B-mCherry plasmid was a gift from Dr. Jennifer Lippincott-Schwartz (Janelia Research Campus).

Cell lines—NIH3T3, L929, MEF and immortalized macrophages (iMacs) were maintained at 37°C, 5% v/v CO₂ in a humidified incubator in DMEM (GIBCO) supplemented with 10% FBS, 2 mM L-glutamine (GIBCO), 200 U/mL penicillin—streptomycin (GIBCO) and 25 μ g/mL plasmocin (Invivogen). HT-29 cells were cultured using the same conditions except McCoy’s 5A media (GIBCO). Jurkat cells were cultured in RPMI-1640 media (GIBCO) with the same supplements as above. All media and supplements were purchased from Life Technology. The HT-29 and Jurkat cell lines are authenticated by the University of Arizona Genetics Core.

RIPK3-2Fv-NIH3T3 cells were previously described (Yatim et al., 2015). The hMLKL¹⁻¹⁸¹-2Fv-NIH3T3 and mMLKL-mCherry-MEF^{Mkl^{-/-}} cell lines were generated by retroviral transduction and mCherry sorting. The Flag-MLKL-NIH3T3^{Mkl^{-/-}} cell line was generated by retroviral transduction and GFP sorting. Briefly, Phoenix-ECO virus producer cells were transfected with the indicated plasmid by using Lipofectamine™ 2000 (Life Technologies) for 72 h. Target cells were infected with filtered virus containing supernatants from packaging cells supplemented with 8 μ g/mL polybrene. Infected cells were spun at 3,000 rpm for 90 min before put back to the incubator. Stable transductants were selected at 72 h post infection by FACS.

The MEF^(Mkl^{-/-}) and hMLKL¹⁻¹⁴⁰-2Fv-Venus-MEF^(Mkl^{-/-}) cell line were described previously (Quarato et al., 2016). NIH3T3^(Mkl^{-/-}), L929^(Mkl^{-/-}) and HT-29^(Mkl^{-/-}) cell lines were generated by CRSPR/Cas9 plasmid pSpCas9(BB)-2A-GFP (PX458). Three targeting guide RNAs were used together to target the region of the murine MLKL initiation codon. The sequences used were TTGGGACAGATCATCAAGTT, CGGAAACAATGCCAGCGTCT and CACACTGTTCATAGATGAGC. Two targeting guide RNAs were used for targeting human MLKL. The sequences used were TAGCCAAGTAGTGAATATGC and GCATATTATCACCTTGGCC. After transfection,

GFP positive cells were collected by FACS and treated overnight with 20 ng/mL TNF α and 100 μ M zVAD (murine cell lines) or 50 ng/mL TNF α , 10 μ M Lcl-161 and 100 μ M zVAD (HT-29). The final survivors were subjected to single cell culture and the MLKL deleted colonies were verified by western blot.

The TMEM16F gene knockout mouse was obtained from Dr. Florian Winau (Boston Children's Hospital). Heterozygous male and female were crossed to obtain littermate wild type, heterozygous, and null embryos. The mouse embryonic fibroblasts were prepared from E10.5–E11.5 embryos. The resulting primary MEFs were transformed with E1A/RAS expressing retroviruses (Quarato et al., 2016).

siRNA—All of the “on-target” siRNA (smart-pool) were purchased from Dharmacon, except CHMP1B (smart-pool) that was obtained from Qiagen. siRNA transfection was performed by Lipofectamin RNAiMax (Life technology) on HT-29 and NIH3T3 cells and INTERFERin (polyplus transfection) on L929 and iMacs, respectively. RNAi efficiency was assessed by realtime PCR at 60 h post transfection or western blot at 72 h post transfection.

Human living donor kidney samples—The human study was approved by the regional committee of ethics in Stockholm (nr 2011/1869-31/4) and adhered to the statutes of the Declaration of Helsinki. Informed consent was obtained from all subjects prior to inclusion in the study. All patients signed informed consent before renal biopsies were obtained at the Karolinska Institute, Stockholm, Sweden.

Paired human kidney biopsies (gender and age listed below) were obtained from 10 living donor kidneys during transplantation at the Karolinska University Hospital, Stockholm, Sweden, before and after the kidneys had been exposed to ischemia-reperfusion. (With a confidence interval of 20 and a population of 10 (matched pairs) and a confidence interval of 95%, the minimal sample size needed is 7 according to this calculator: <http://www.surveysystem.com/sscalc.htm>). The gender and ages of the ten kidney donors were M, 29.6; M, 39.0; M, 45.4; M, 46.3; M, 50.4; F, 38.1; F, 39.4; F, 43.1; F, 51.9; and F, 53.7.

The first biopsy (baseline) was taken no later than 5 min. after removal of the kidney from the donor, and the second biopsy (ischemia-reperfusion) after 3-15 min of warm ischemia, 1-2 h of cold ischemia, and 1 h of reperfusion in the recipient.

Animal models—For the xenograft tumor model, immune deficient *Rag-1*^{-/-} mice (equally mixed gender, 2-4 months) were intradermally injected (i.d.) with 100 μ L, 5×10^5 RIPK3-2Fv-NIH3T3 (resuspended in PBS) with scramble siRNA or CHMP2A siRNA. In the B/B treated groups, 8×10^5 B/B induced Annexin V⁺ SytoxGreen⁻ RIPK3-2Fv-NIH3T3 with scramble siRNA or CHMP2A siRNA were sorted and resuscitated briefly by washout ligand for 45 min before intradermal injection. Tumor volumes were measured with calipers two weeks after injection (Tumor volume= length \times width²/2).

The assessment of *in vivo* cross-priming of CD8⁺ T cells was adapted from a recent report (Yatim et al., 2015). RIPK3-2Fv-NIH3T3 (H-2^d) cells were transfected with siRNA at 72 h and the Tfr-ovalbumin (OVA)-expressing plasmid at 48 h before injection into mice.

Alternatively, cells were stably transduced with OVA and the plasmid transfection was skipped. B/B dimerizer was added to RIPK3-2Fv-NIH3T3 cells (500 nM) for 25 min at 37°C. Then 10^6 cells were washed once with PBS and injected into C57BL/6 mice (equally mixed gender, 2–4 months, H-2^b) intra-dermally (i.d.) into the flank of each mouse. 9 days later, the draining lymph nodes (inguinal lymph nodes) were harvested and stained with anti-CD8a-APC and SIINFEKL-pentamer-PE (Proimmune) before analysis with a flow cytometry FACsCalibur system (BD Biosciences). Cells with both CD8a⁺ and SIINREKL-pentamer⁺ were counted as cross-primed cells. Data are presented as either individual lymph nodes or individual mice, as indicated in the Figure Legends.

All animals were housed in temperature- and humidity-controlled conditions on a 12 h/12 h light/dark cycle with *ad lib* access to food and water in our institutional animal facility. No animals had been involved in any previous procedures before this study and all were drug or test naïve. All animals were randomly assigned to experimental treatment groups. All animals in each treatment groups were included in final analysis. All experiments were done in accordance with the Guide for the Care and Use of Laboratory Animals, and the St. Jude Children's Research Hospital Animal Care and Use Committee approved all animal procedures.

METHOD DETAILS

Flow cytometric quantification of cell death—All *in vitro* experiments assessed by flow cytometry included at least triplicate cultures for each condition (n = 3), and data shown are representative of at least two independent experiments. To assess necroptosis or apoptosis, cells were trypsinized, resuspended in serum-free DMEM and stained with Annexin V-APC (1:50, eBioscience), 50 nM SytoxGreen (invitrogen) or 2 µg/ml PI (Sigma) for 5 min. Alternatively, cells were stained with Annexin V-FITC (1:50, eBioscience) or MFG-E8-FITC (1:50, Haematologic Technologies) and TO-PRO[®]-3 (500 nM, Molecular Probes).

Cells with Annexin-V^{+/−}, PI^{+/−}, TO-PRO[®]-3^{+/−} or SytoxGreen^{+/−} were analyzed by flow cytometry using FACScan or FACsCalibur systems (BD Biosciences) and FlowJo Collectors' Edition software (Tree Star). The percentages of differently labeled cells were calculated by FlowJo software (Tree Star).

Cell resuscitation assay—RIPK3-2Fv-NIH3T3 cells were trypsinized and resuspended in completed DMEM culture media and stimulated with 25 nM B/B for 45 min at 37°C, gently flicking the tube every 5-10 min. Annexin V-APC (1:40, eBioscience) and 50 nM SytoxGreen (invitrogen) was added to label the cells for 2 min at room temperature, which were then sorted by Reflection (i-Cyt, SONY). The sorted Annexin V⁺, SytoxGreen[−] cells were re-plated with 25 nM B/B (B/B), complete media alone (control), or 3 µM washout ligand (washout) for 7 h, as indicated. The cells were then re-suspended and stained again as above. Cell death was analyzed by flow cytometry, using FACScan or FACsCalibur systems (BD Biosciences) and FlowJo Collectors' Edition software (Tree Star). For hMLKL^{1–181}-2Fv-NIH3T3 cells, 50 nM B/B was used to stimulate necroptosis. The dying cells were stained and sorted as above, followed by re-plating with 25 nM B/B, complete

media (control), 3 μ M washout ligand, or 5 μ M NSA for 6h, as indicated. Cell death was then assessed as above. For RIPK3-2Fv-iMacs cells and HT-29 cells, cell death was induced before trypsinization. RIPK3-2Fv-iMacs cells were treated with 25 nM B/B for 120 min. HT-29 cells were treated with 50ng/mL TNF α , 10 μ M Lcl-161, and 100 μ M zVAD (TSZ) for 2 h. Then the cells were trypsinized, stained and sorted as above. The Annexin-V⁺ SytoxGreen⁻ RIPK3-2Fv-iMacs cells were then re-cultured with 25 nM B/B, complete media (control) or 3 μ M washout ligand for 7 h, as indicated. The Annexin-V⁺ SytoxGreen⁻ HT-29 cells were then treated with TSZ, complete media (control) or 5 μ M NSA for 7 h, as indicated. The cell death was analyzed as above. For Jurkat cells, the cell death was induced by TSZ for 3.5 h, after which cells were sorted, treated and analyzed as above.

Real-time PCR—Total RNA for real-time PCR was extracted and purified using the RNeasy Mini Kit (Qiagen). Reverse transcription reactions were performed with M-MLV reverse transcriptase (Life Technology), following the standard protocol using random hexamers (IDT). Real-time PCR was performed with SYBRTM Green labeling in 7500 Fast RealTime PCR System (Applied Biosystems). PCR conditions were 50°C for 2 min, 95°C for 10 min, and 45 cycles of 95°C for 15 s and 60°C for 1 min. mRNA expression was normalized against β -actin, allowing comparison of mRNA levels. Primers used in this study are listed in Table S3.

IncuCyte Analysis—For IncuCyte analysis, cells were first seeded into 6, 12, or 24-well plates for overnight incubation. 50 nM SytoxGreen (Molecular Probes) plus the indicated cell death stimuli were added, and the cells were moved into an IncuCyte live cell imaging system (<http://www.essenbioscience.com/en/products/incucyte/?gclid=CJ7ywJynytlCFd63wAodCeEALA>). Cells were imaged every 1 h and the SytoxGreen labeled cells (counted as dead cells) were quantified by the IncuCyte FLR or Zoom software (<http://www.essenbioscience.com/en/products/software/>). Alternatively, to measure the Ca⁺⁺ influx, cells expressing GCaMP3 were used. For this purpose, cells were cultured with the indicated stimuli without SytoxGreen. GCaMP3 fluorescence intensity within the cells, recorded by the IncuCyte live cell imaging system, indicated the Ca⁺⁺ influx.

When percentages are shown, total cell number was quantified at the end of each course of treatment, using 200 μ g/ml digitonin (Sigma-Aldrich) to permeabilize all cells which were stained with 50 nM SytoxGreen. Data were then expressed as a percentage of SytoxGreen⁺ cells to total cell numbers. At least two experiments were performed with four replicates for each condition.

Clonogenic growth—Sorted AnnexinV⁺ SytoxGreen⁻ cells (see “Cell resuscitation assay”) were seeded in 12 well plates with or without indicated treatment. After 10-14 days in culture, the plates were gently washed once with PBS and then stained with methylene blue solution (1% w/v methylene blue in a 50:50 methanol/water solution, methylene blue was purchased from Sigma-Aldrich.) for 30 min at room temperature. The plates were then carefully washed with dH₂O and allowed to air dry. The plates were scanned using a document scanner and images are shown.

Confocal microscopy—Cells were plated on 2-well or 4-well glass chamber slides (Mattek) coated with fibronectin (100 µg/mL in PBS, Millipore). Cells were maintained in complete media at 37°C and 5% CO₂ in an environmentally controlled chamber (Solent Scientific, UK). MFG-E8-FITC (Haematologic Technologies); Annexin V-Alexa Fluor-488 (Molecular Probes); Annexin V-PE (eBioscience); Annexin V-FITC (eBioscience) or Annexin V-Alexa Fluor-647 (Molecular Probes) were added into the media to label PS externalization (1:100). As indicated, DiI (50 µg/mL, Molecular Probes) was added into media for 5 min to label the plasma membrane and then removed by washing twice with complete media. Cells were then stimulated with B/B dimerizer or TSZ before confocal microscopy analysis. Cells with or without plasma membrane bubbles were manually counted.

To measure Dextran uptake, 10 kD Dextran-NH₂-Alexa Fluor 647 (10 µg/mL, Molecular Probes) and Annexin V-Alexa Fluor-488 (molecular probes) were added to the dying cells for 5 min, then immediately fixed with 4% paraformaldehyde (Electron Microscopy Science, diluted in serum free DMEM with additional 5 mM CaCl₂) for 10 min at room temperature. Then the cells were washed once with serum free DMEM and examined by confocal microscopy.

To measure GFP-CHMP4B translocation, the GFP-CHMP4B plasmids were transfected into NIH3T3 or MEF cells with Lipofectamine LTX & PLUSTM Reagent (Invitrogen). 24 h post transfection, the 40% low fraction of GFP⁺ cells were sorted and seeded onto glass chamber slides described above. The cells were analyzed by confocal microscopy the next day, upon addition of dimerizer as described above. Cells with or without GFP-CHMP4B translocation were manually counted.

To measure Ca⁺⁺ influx, the GCaMP3 probe was expressed in the indicated cell lines by retrovirus-mediated transduction. The GCaMP3 intensity was recorded to indicate Ca⁺⁺ influx upon treatment, as indicated.

Confocal microscopy was performed with a Marianas spinning disk confocal imaging system (Intelligent Imaging Innovations/3i) consisting of a CSU-22 confocal head (Yokogawa Electric Corporation, Japan); solid-state diode-pumped laser launch (3i) with wavelengths of 445 nm, 473 nm, 523 nm, 561 nm, and 658 nm; and a Carl Zeiss Axiovert 200M motorized inverted microscope equipped with a precision motorized XY stage (Carl Zeiss MicroImaging) and spherical aberration correction optics (3i). The images were analyzed with Slidebook 6.

Transmission electron microscopy—After B/B stimulation, NIH3T3 cells are fixed in 2.5% glutaraldehyde and 2% paraformaldehyde in 0.1 M sodium cacodylate buffer pH 7.4 before post-fixation in 2% osmium tetroxide in 0.1 M cacodylate buffer with 0.15% potassium ferrocyanide. After rinsing in buffer the tissue was dehydrated through a series of graded ethanol to propylene oxide, infiltrated and embedded in epoxy resin and polymerized at 70°C overnight. Semi-thin sections (0.5 micron) are stained with toluidine blue for light microscope examination. Ultrathin sections (80 nm) are cut and imaged using the Tecnai

TF20 TEM with an AMT XR41 camera. TEM images were acquired using A FEI Tecnai 20 200KV FEG Electron Microscope.

Determination of membrane-bound MLKL and CHMP4B—hCHMP4B-mCherry was stably expressed in RIPK3-2Fv-NIH3T3 or hMLKL¹⁻¹⁴⁰-2Fv-Venus-MEF^{MLKL^{-/-}} cells. For the MEF cells, 2 µg/mL Dox was added overnight for induction of MLKL¹⁻¹⁴⁰ expression. Membrane bound MLKL and CHMP4B were measured with a digitonin based flow cytometric assay. After treatment (e.g. 100 nM B/B for 30 min), cells were permeabilized with 200 µg/mL digitonin for 5 min at room temperature. Then the cells were washed once with PBS before assessment by flow cytometry. After permeabilization, free cytosolic MLKL or CHMP4B is lost, while the membrane associated portion remains. FACS analysis was performed to determine the amount of fluorescent signal remaining after digitonin permeabilization. MFI (mean fluorescent intensity) was calculated from triplicate samples.

Cytokine and chemokine detection—Supernatants from treated cells were collected (as indicated in Figure 5). Cell debris was removed by centrifugation at 6,000 rpm for 1 min. Samples were diluted with the dilution buffer provided in each ELISA kit, including murine CXCL10 ELISA (eBioscience), murine CXCL1 (R & D) and murine TNFα (R & D). All experiments were performed in triplicate.

IL-1α, IL-1β, IL-6, CXCL10 and TNFα analysis was performed using the Luminex technologies (Millipore) bead-based flow cytometry technique according to the users manual. All experiments were performed in triplicate cultures.

Western Blotting—Cells were lysed with loading buffer (50 mM Tris pH=6.8, 2%SDS and 10% glycerol) and denatured by boiling. Protein concentration was then determined by the BCA assay (Pierce) and systematically normalized before SDS-PAGE. Following the transfer of proteins to Hybond C nitrocellulose (Amersham Bioscience), immunodetection was performed using the indicated primary and peroxidase-coupled secondary antibodies (Amersham Bioscience). Proteins were visualized by enhanced chemiluminescence (ECL, Amersham Bioscience).

For p-MLKL detection in HT-29 cells, the antibody ab187091 (Abcam) was used. For p-MLKL detection in iMac cells, the antibody ab196436 (Abcam) was used. For p-MLKL detection in NIH3T3 cells, a construct expressing a “humanized” mouse MLKL was retrovirally introduced. In this construct, the human MLKL sequence “ELRKTQTSM^{SL}GTTR” replaced the mouse MLKL sequence “ELSKTQNSISRTAKS”. This “humanized” mouse MLKL is phosphorylated by mouse RIPK3 and is also recognized by human p-MLKL antibody ab187091 (Abcam).

Histology and immunohistochemistry of renal biopsies—Biopsies were dissected as indicated in each experiment and infused with 4% neutral-buffered formaldehyde, fixed for 48 h, dehydrated in a graded ethanol series and xylene, and finally embedded in paraffin. Paraffin sections (3–5 mm) were stained with periodic acid–Schiff reagent, according to the standard routine protocol. Immunohistochemistry for S358 pMLKL monoclonal antibody

(Abcam, EPR9514) was performed according to routine protocols with dilutions of 1:500 to 1:1000. Micrographs were digitalized using an AxioCam MRm Rev. 3 FireWire camera and AxioVision Rel. 4.5 software (Zeiss). The percentage of the number of pMLKL⁺ cells to the total number of the endothelial cells was quantified by an experienced pathologist in a double-blind manner (that is, all slides were randomized and coded, independently of individual patient sample or treatment).

RNA extraction and library construction—The biopsy samples were immediately placed in RNazol before subsequent microdissection into tubulointerstitial and glomerular fractions. Total RNA was extracted from the tubulointerstitial fraction using a QIAcube robot (Qiagen, Netherlands). Quality control was performed on a Agilent Tapestation 2200 (Agilent Technologies, Inc., CA, US). cDNA libraries were prepared with a Illumina TruSeq Stranded mRNA kit using Poly-A selection.

Sequencing—Clustering was done by ‘cBot’ and samples were sequenced on HiSeq2500 (HiSeq Control Software 2.2.58/RTA 1.18.64) with a 2×126 setup using ‘HiSeq SBS Kit v4’ chemistry. The Bcl to FastQ conversion was performed using bcl2fastq-1.8.4 from the CASAVA software suite. The quality scale used is Sanger/phred33/Illumina 1.8+. Average sequencing depth was 34.4 million reads per sample.

Data processing—Raw sequencing reads were processed to obtain counts per genes for each sample. This included: 1. FastQC/0.11.2 quality check on raw sequencing reads; 2. Trimmomatic/0.32 reads filtering for quality score and read length. Reads with average quality below 20 (within 4-base wide sliding window) and/or shorter than 36 bases were removed; 3. Star/2.4.1c was used to align the reads to the reference genome Homo_sapiens.GRCh38-dna.primary_assembly.fa using the annotation Homo_sapiens.GRCh38.83.gtf, with reference genome and annotation downloaded from <http://www.ensembl.org/index.html>. FeatureCounts/1.5.0 from subread/1.4.5 was used to count the fragments in the exon regions as defined in the Homo_sapiens.GRCh38.83.gtf file, using default parameters. Specifically, for paired-end reads, a fragment is said to overlap a feature if at least one read base is found to overlap the feature. Fragments overlapping with more than one feature and multi-mapping reads were not counted. Counts from multiple lanes were added, if applicable. Samtools/0.1.19 was used to sort and index the BAM files containing the aligned reads, e.g. for visualization in IGV genome browser. QualiMap/2.2 was used to evaluate the quality of the alignment data. MultiQC/0.3.1 was used to aggregate results from FastQC/0.11.2, star/2.4.1c and featureCounts/1.5.0 across many samples into a single report.

Differential expression—All analyses were performed under R, a programming language and software environment for statistical computing and graphics. The BiomaRt package was used to annotate Ensembl gene identifiers with chromosome name, official gene symbol and description. Low count reads were filtered by keeping reads with at least 1 read per million in at least 2 samples. The EdgeR package was used to normalize for the RNA composition by finding a set of scaling factors for the library sizes that minimize the log-fold changes between the samples for most genes, using a trimmed mean of M values

(TMM) between each pair of samples. The normalized counts were used to examine the samples for outliers and relationships, using Multidimensional Scaling and heatmap based on the Pearson correlation coefficient between every sample pair. The EdgeR package was used to define design matrix based on the experimental design, fitting genewise glms model and conducting likelihood ratio tests for the selected group comparisons.

QUANTIFICATION AND STATISTICAL ANALYSIS

Statistical tests were done using Microsoft Excel and Prism. The statistical test used and p values were indicated within each figure. Generally, for comparison between two individual groups, standard student t-test was used. For comparison of more than two groups, standard one-way ANOVA was used. The number of repeats of each experiment was indicated within each figure as well. Data are presented as means \pm SD or SEM (indicated within each figure). p values less than 0.05 were considered statistically significant.

No methods were applied to determine whether the data met assumptions of the statistical approach used. Normal distributions were assumed. No strategy for randomization and/or stratification method was applied in this study.

DATA AND SOFTWARE AVAILABILITY

The mRNA array data for B/B induced hMLKL¹⁻¹⁸¹-2Fv-NIH3T3 cells are GEO: GSE85660. The human kidney biopsies RNA-seq data are uploaded to <https://www.obvibase.com/#token/cHluy8Hv4Cdb/r/hka6j0CQmzwp>

Supplementary Material

Refer to Web version on PubMed Central for supplementary material.

Acknowledgments

We thank Paul Bieniasz, Florian Winau, Giovanni Quarato, Jennifer Lippincott-Schwartz, Andrew Oberst and Helen Beere for valuable mice and reagents; Helen Beere, Ruoning Wang, Hu Zeng, and Qifan Zhu for helpful discussions; Richard Cross, Greig Lennon, Parker Ingle, and Tammar Williams for cell sorting; Melanie Loyd and David Finkelstein for mRNA array analysis; Susu Duan for RNA-seq data visualization; and Sharon Frase for TEM. This work was supported by grants from the US NIH, ALSAC, and the cluster of excellence EXC306 (to AL).

References

- Albert ML, Sauter B, Bhardwaj N. Dendritic cells acquire antigen from apoptotic cells and induce class I-restricted CTLs. *Nature*. 1998; 392:86–89. [PubMed: 9510252]
- Andrews NW, Almeida PE, Corrotte M. Damage control: cellular mechanisms of plasma membrane repair. *Trends Cell Biol*. 2014; 24:734–742. [PubMed: 25150593]
- Carlton J. The ESCRT machinery: a cellular apparatus for sorting and scission. *Biochem Soc Trans*. 2010; 38:1397–1412. [PubMed: 21118097]
- Choudhuri K, Llodra J, Roth EW, Tsai J, Gordo S, Wucherpfennig KW, Kam LC, Stokes DL, Dustin ML. Polarized release of T-cell-receptor-enriched microvesicles at the immunological synapse. *Nature*. 2014; 507:118–123. [PubMed: 24487619]
- Christ L, Raiborg C, Wenzel EM, Campsteijn C, Stenmark H. Cellular Functions and Molecular Mechanisms of the ESCRT Membrane-Scission Machinery. *Trends Biochem Sci*. 2017; 42:42–56. [PubMed: 27669649]

- Dasgupta SK, Guchhait P, Thiagarajan P. Lactadherin binding and phosphatidylserine expression on cell surface-comparison with annexin A5. *Transl Res.* 2006; 148:19–25. [PubMed: 16887494]
- Degterev A, Maki JL, Yuan J. Activity and specificity of necrostatin-1, small-molecule inhibitor of RIP1 kinase. *Cell Death Differ.* 2013; 20:366. [PubMed: 23197295]
- Dillon CP, Oberst A, Weinlich R, Janke LJ, Kang TB, Ben-Moshe T, Mak TW, Wallach D, Green DR. Survival function of the FADD-CASPASE-8-cFLIP(L) complex. *Cell Rep.* 2012; 1:401–407. [PubMed: 22675671]
- Jimenez AJ, Maiuri P, Lafaurie-Janvore J, Divoux S, Piel M, Perez F. ESCRT machinery is required for plasma membrane repair. *Science.* 2014; 343:1247136. [PubMed: 24482116]
- Kaiser WJ, Upton JW, Long AB, Livingston-Rosanoff D, Daley-Bauer LP, Hakem R, Caspary T, Mocarski ES. RIP3 mediates the embryonic lethality of caspase-8-deficient mice. *Nature.* 2011; 471:368–372. [PubMed: 21368762]
- Kang S, Fernandes-Alnemri T, Rogers C, Mayes L, Wang Y, Dillon C, Roback L, Kaiser W, Oberst A, Sagara J, et al. Caspase-8 scaffolding function and MLKL regulate NLRP3 inflammasome activation downstream of TLR3. *Nat Commun.* 2015; 6:7515. [PubMed: 26104484]
- Kang TB, Yang SH, Toth B, Kovalenko A, Wallach D. Caspase-8 blocks kinase RIPK3-mediated activation of the NLRP3 inflammasome. *Immunity.* 2013; 38:27–40. [PubMed: 23260196]
- Lawlor KE, Khan N, Mildenhall A, Gerlic M, Croker BA, D'Cruz AA, Hall C, Kaur Spall S, Anderton H, Masters SL, et al. RIPK3 promotes cell death and NLRP3 inflammasome activation in the absence of MLKL. *Nat Commun.* 2015; 6:6282. [PubMed: 25693118]
- Leventis PA, Grinstein S. The distribution and function of phosphatidylserine in cellular membranes. *Annu Rev Biophys.* 2010; 39:407–427. [PubMed: 20192774]
- Liu J, Krautberger AM, Sui SH, Hofmann OM, Chen Y, Baetscher M, Grgic I, Kumar S, Humphreys BD, Hide WA, et al. Cell-specific translational profiling in acute kidney injury. *J Clin Invest.* 2014; 124:1242–1254. [PubMed: 24569379]
- Mahul-Mellier AL, Strappazon F, Petiot A, Chatellard-Causse C, Torch S, Blot B, Freeman K, Kuhn L, Garin J, Verna JM, et al. Alix and ALG-2 are involved in tumor necrosis factor receptor 1-induced cell death. *J Biol Chem.* 2008; 283:34954–34965. [PubMed: 18936101]
- Maminska A, Bartosik A, Banach-Orlowska M, Pilecka I, Jastrzebski K, Zdzalik-Bielecka D, Castanon I, Poulain M, Neyen C, Wolinska-Nizioł L, et al. ESCRT proteins restrict constitutive NF-kappaB signaling by trafficking cytokine receptors. *Sci Signal.* 2016; 9:ra8. [PubMed: 26787452]
- Martin SJ, Reutelingsperger CP, McGahon AJ, Rader JA, van Schie RC, LaFace DM, Green DR. Early redistribution of plasma membrane phosphatidylserine is a general feature of apoptosis regardless of the initiating stimulus: inhibition by overexpression of Bcl-2 and Abl. *J Exp Med.* 1995; 182:1545–1556. [PubMed: 7595224]
- Matusek T, Wendler F, Poles S, Pizette S, D'Angelo G, Furthauer M, Therond PP. The ESCRT machinery regulates the secretion and long-range activity of Hedgehog. *Nature.* 2014; 516:99–103. [PubMed: 25471885]
- McCullough J, Clippinger AK, Talledge N, Skowrya ML, Saunders MG, Naismith TV, Colf LA, Afonine P, Arthur C, Sundquist WI, et al. Structure and membrane remodeling activity of ESCRT-III helical polymers. *Science.* 2015; 350:1548–1551. [PubMed: 26634441]
- Oberst A, Dillon CP, Weinlich R, McCormick LL, Fitzgerald P, Pop C, Hakem R, Salvesen GS, Green DR. Catalytic activity of the caspase-8-FLIP(L) complex inhibits RIPK3-dependent necrosis. *Nature.* 2011; 471:363–367. [PubMed: 21368763]
- Orozco S, Yatim N, Werner MR, Tran H, Gunja SY, Tait SW, Albert ML, Green DR, Oberst A. RIPK1 both positively and negatively regulates RIPK3 oligomerization and necroptosis. *Cell Death Differ.* 2014; 21:1511–1521. [PubMed: 24902904]
- Quarato G, Guy CS, Grace CR, Llambi F, Nourse A, Rodriguez DA, Wakefield R, Frase S, Moldoveanu T, Green DR. Sequential Engagement of Distinct MLKL Phosphatidylinositol-Binding Sites Executes Necroptosis. *Mol Cell.* 2016; 61:589–601. [PubMed: 26853145]
- Scheffer LL, Sreetama SC, Sharma N, Medikayala S, Brown KJ, Defour A, Jaiswal JK. Mechanism of Ca(2+)-triggered ESCRT assembly and regulation of cell membrane repair. *Nat Commun.* 2014; 5:5646. [PubMed: 25534348]

- Segawa K, Kurata S, Yanagihashi Y, Brummelkamp TR, Matsuda F, Nagata S. Caspase-mediated cleavage of phospholipid flippase for apoptotic phosphatidylserine exposure. *Science*. 2014; 344:1164–1168. [PubMed: 24904167]
- Sun L, Wang H, Wang Z, He S, Chen S, Liao D, Wang L, Yan J, Liu W, Lei X, et al. Mixed lineage kinase domain-like protein mediates necrosis signaling downstream of RIP3 kinase. *Cell*. 2012; 148:213–227. [PubMed: 22265413]
- Suzuki J, Denning DP, Imanishi E, Horvitz HR, Nagata S. Xk-related protein 8 and CED-8 promote phosphatidylserine exposure in apoptotic cells. *Science*. 2013; 341:403–406. [PubMed: 23845944]
- Suzuki J, Umeda M, Sims PJ, Nagata S. Calcium-dependent phospholipid scrambling by TMEM16F. *Nature*. 2010; 468:834–838. [PubMed: 21107324]
- Vanden Berghe T, Hassannia B, Vandenabeele P. An outline of necrosome triggers. *Cell Mol Life Sci*. 2016; 73:2137–2152. [PubMed: 27052312]
- Wallach D, Kang TB, Dillon CP, Green DR. Programmed necrosis in inflammation: Toward identification of the effector molecules. *Science*. 2016; 352:aaf2154. [PubMed: 27034377]
- Wang H, Sun L, Su L, Rizo J, Liu L, Wang LF, Wang FS, Wang X. Mixed lineage kinase domain-like protein MLKL causes necrotic membrane disruption upon phosphorylation by RIP3. *Mol Cell*. 2014a; 54:133–146. [PubMed: 24703947]
- Wang X, Jiang W, Yan Y, Gong T, Han J, Tian Z, Zhou R. RNA viruses promote activation of the NLRP3 inflammasome through a RIP1-RIP3-DRP1 signaling pathway. *Nat Immunol*. 2014b; 15:1126–1133. [PubMed: 25326752]
- Weinlich R, Green DR. The two faces of receptor interacting protein kinase-1. *Mol Cell*. 2014; 56:469–480. [PubMed: 25459879]
- Weinlich R, Oberst A, Beere HM, Green DR. Necroptosis in development, inflammation and disease. *Nat Rev Mol Cell Biol*. 2017; 18:127–136. [PubMed: 27999438]
- Xie T, Peng W, Yan C, Wu J, Gong X, Shi Y. Structural insights into RIP3-mediated necroptotic signaling. *Cell Rep*. 2013; 5:70–78. [PubMed: 24095729]
- Yatim N, Jusforgues-Saklani H, Orozco S, Schulz O, Barreira da Silva R, Reis e Sousa C, Green DR, Oberst A, Albert ML. RIPK1 and NF-kappaB signaling in dying cells determines cross-priming of CD8(+) T cells. *Science*. 2015; 350:328–334. [PubMed: 26405229]
- Yoon S, Bogdanov K, Kovalenko A, Wallach D. Necroptosis is preceded by nuclear translocation of the signaling proteins that induce it. *Cell Death Differ*. 2016; 23:253–260. [PubMed: 26184911]
- Zhang J, Yang Y, He W, Sun L. Necrosome core machinery: MLKL. *Cell Mol Life Sci*. 2016; 73:2153–2163. [PubMed: 27048809]

HIGHLIGHTS

Phosphatidylserine is exposed prior to loss of cell integrity during necroptosis.

ESCRT-III facilitates the shedding of MLKL-damaged plasma membrane from intact cells.

ESCRT-III supports cell survival and functions downstream of active MLKL.

ESCRT-III allows necroptotic cells to signal surrounding cells.

In brief

Cells undergoing necroptosis aren't always headed toward death; ESCRT-III helps preserve the plasma membrane in these cells contributing toward survival.

Author Manuscript

Author Manuscript

Author Manuscript

Author Manuscript

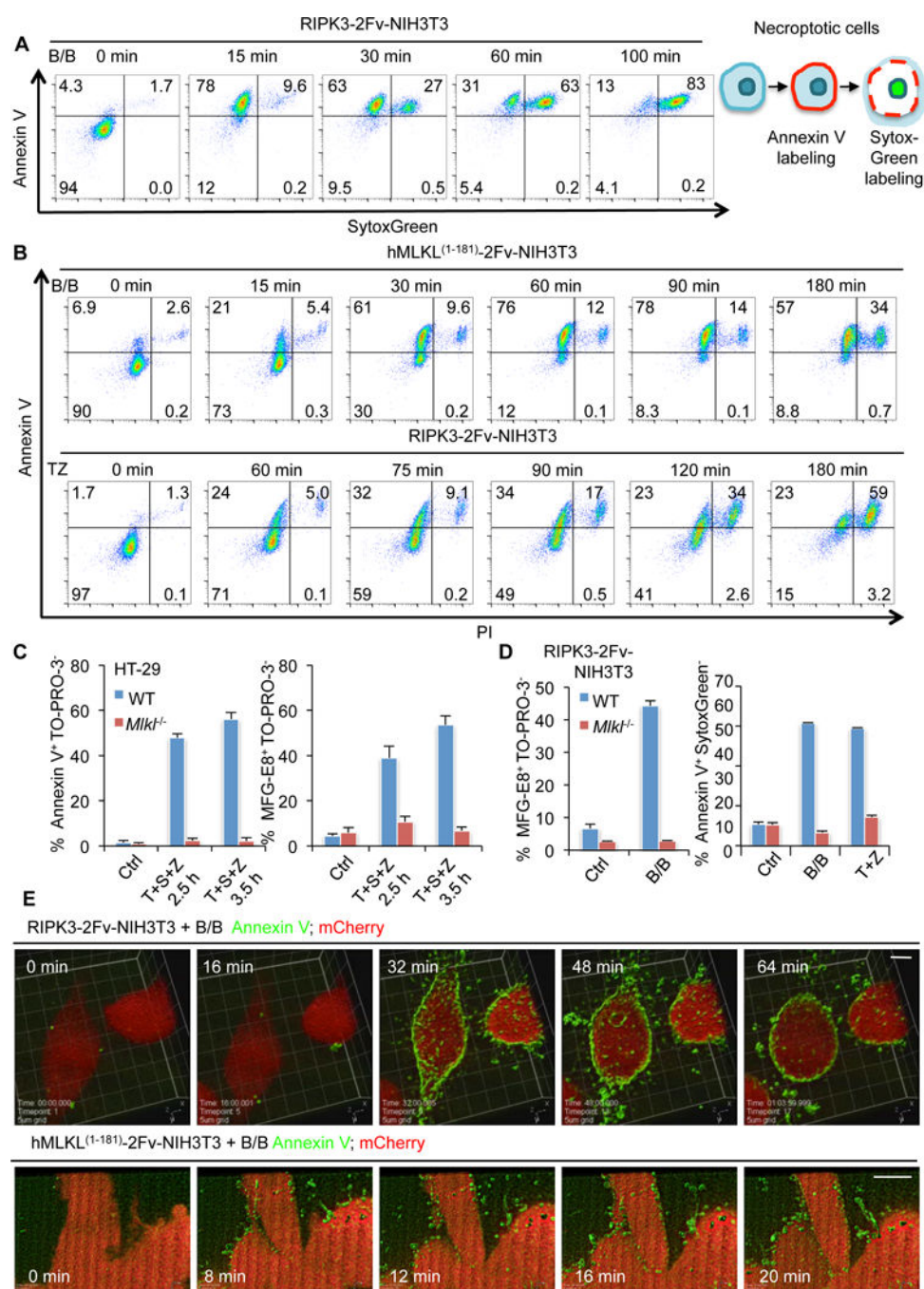


Figure 1. PS externalization occurs prior to loss of plasma membrane integrity during necroptosis

(A) Flow cytometric analysis of 100 nM B/B dimerizer-treated RIPK3-2Fv-NIH3T3 cells stained with SytoxGreen and AnnV-APC at the indicated time points.

(B) Flow cytometric analysis of hMLKL¹⁻¹⁸¹-2Fv-NIH3T3 cells treated with 100 nM B/B dimerizer (upper panels) or RIPK3-2Fv-NIH3T3 cells treated with 20 ng/mL TNF α plus 100 μ M zVAD (TZ) (lower panels). Cells were stained with AnnV-APC and PI at the indicated time points.

(C) HT-29 cells (WT or *Mik1^{-/-}*) were treated with 50 ng/mL TNF α , 10 μ M Lcl-161, and 100 μ M zVAD (TSZ) for the indicated times. PS exposure was assessed by AnnV-FITC and TO-PRO-3 or MFG-E8-FITC and TO-PRO-3 staining before analysis by flow cytometry.

(D) RIPK3-2Fv-NIH3T3 cells (WT or *Mik1^{-/-}*) were treated with 100 nM B/B for 30 min or TZ for 90 min. PS exposure was assessed as in (C).

(E) Time lapsed, Z-stacked confocal images of 100 nM B/B treated and AnnV-FITC (green) stained RIPK3-2Fv-NIH3T3 (upper panel) or hMLKL¹⁻¹⁸¹-2Fv-NIH3T3 (lower panel) cells. Cells express mCherry (red) to demarcate cell body. Scale bar=5 μ m (upper panel) and 10 μ m (lower panel).

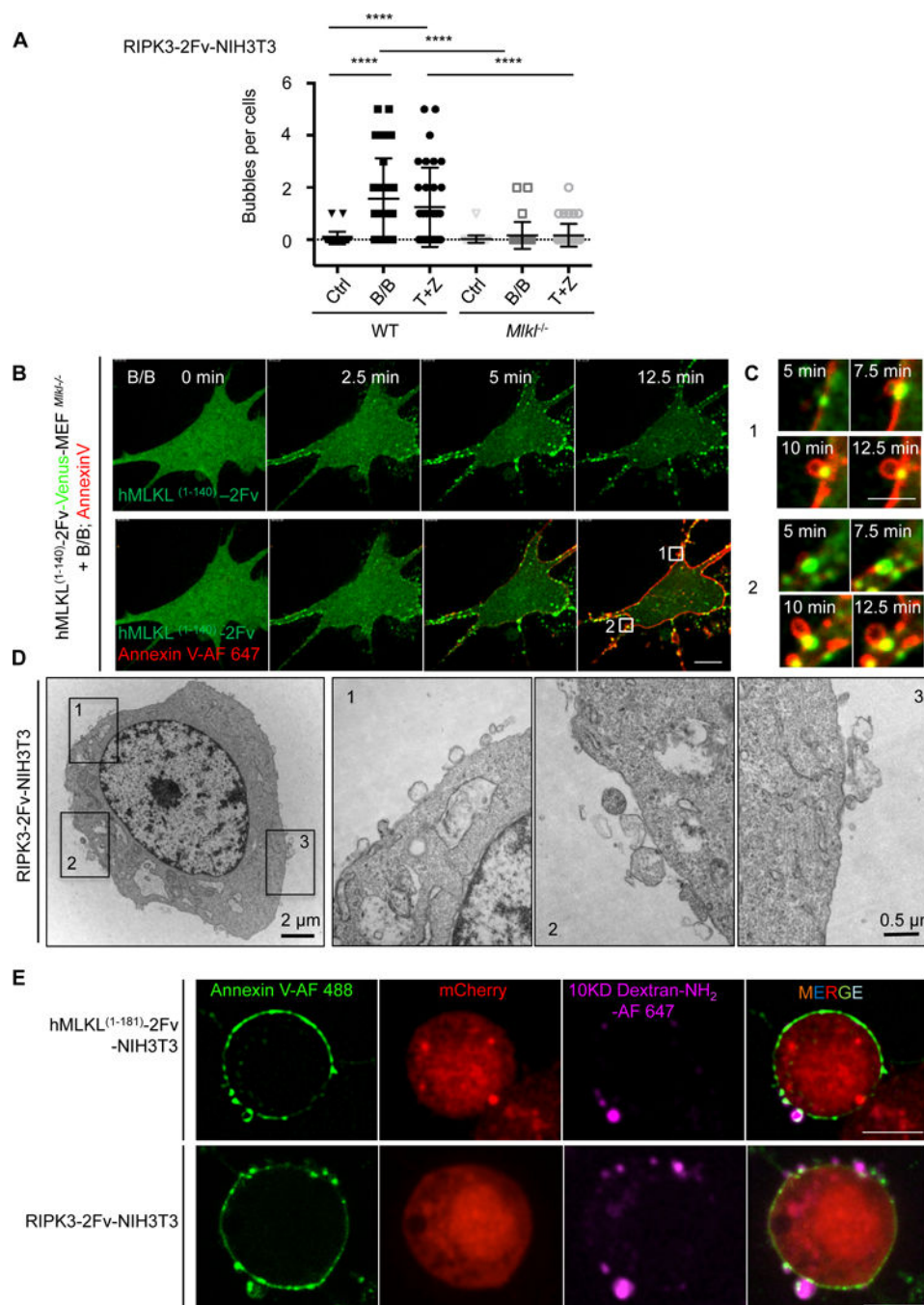


Figure 2. Shedding of PS-exposed plasma membrane bubbles during necroptosis

(A) Quantification of bubble formation. Z-stacked confocal images of DiI stained necroptotic RIPK3-2Fv-NIH3T3 (WT or *Mlkl*^{-/-}) cells were analyzed and bubbles 0.5 μ m were counted. Each point represents one cell analyzed. **** $p < 0.0001$, Student unpaired t-test.

(B) Doxycycline (Dox) inducible hMLKL⁽¹⁻¹⁴⁰⁾-2Fv-Venus-MEF *Mlkl*^{-/-} cells were treated with 2 μ g/mL Dox overnight, followed by addition of 25 nM B/B and AnnV-AF647 (red). Time lapsed images were recorded by confocal microscopy. Scale bar=10 μ m.

(C) Enlarged, time lapsed images of the two regions indicated in (B). Scale bar=1 μm .
(D) Images of B/B treated RIPK3-2Fv-NIH3T3 cells processed for TEM.
(E) Confocal microscope images of hMLKL¹⁻¹⁸¹-2Fv-NIH3T3 (upper panel) and RIPK3-2Fv-NIH3T3 (lower panel) cells, treated with 100 nM B/B. Cells expressed mCherry (red) and were stained with AnnV-AF488 (green) and 10 kD Dextran-NH₂-AF647 (violet). Scale bar=10 μm .

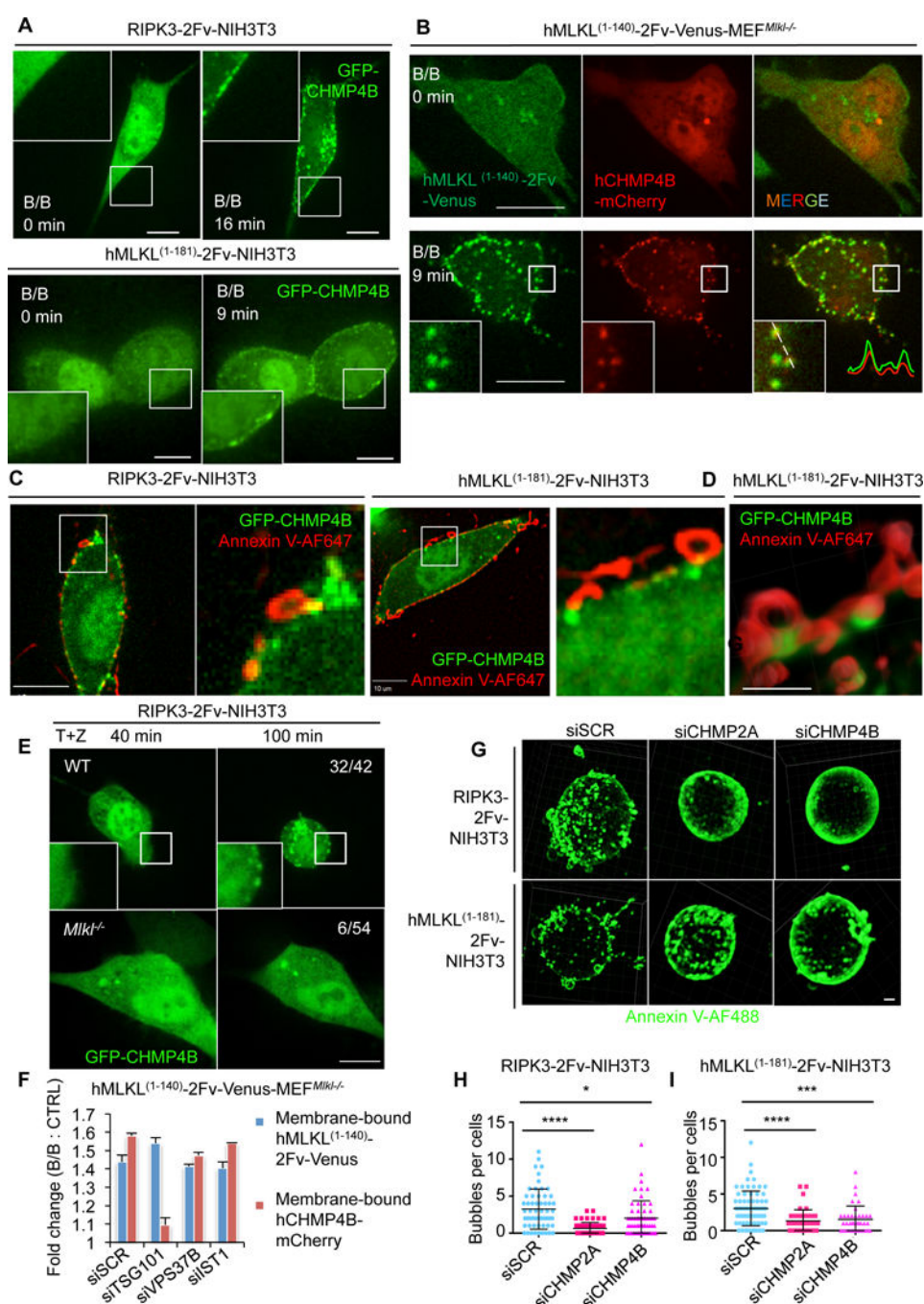


Figure 3. The ESCRT-III machinery mediates plasma membrane shedding during necroptosis
 (A) Confocal microscope images of 100 nM B/B treated, GFP-CHMP4B expressing RIPK3-2Fv-NIH3T3 or hMLKL¹⁻¹⁸¹-2Fv-NIH3T3 cells. Scale bar=10 μ m.
 (B) Dox-inducible hMLKL⁽¹⁻¹⁴⁰⁾-2Fv-Venus (green) in *Mlkl*^{-/-} MEF, transiently transfected with hCHMP4B-mCherry (red), were treated with 2 μ g/mL Dox overnight, followed by 25 nM B/B. Time lapsed images were recorded by confocal microscopy. Scale bar=10 μ m. Insets: (lower left) enlargement of indicated box, (lower right) fluorescent intensities along the dashed line.

(C–D) Confocal microscope images of GFP-CHMP4B-expressing RIPK3-2Fv-NIH3T3 (left panel of C) and hMLKL^{1–181}-2Fv-NIH3T3 (right panel of C and D), treated with 100 nM B/B and stained with AnnV-AF647 (red). Enlargements of the boxed areas are shown in the images on the right. Scale bar=10 μ m. D shows a Z-stacked rendering. Scale bar=1 μ m.

(E) Confocal microscope images of GFP-CHMP4B-expressing RIPK3-2Fv-NIH3T3 (WT and *Mkl1*^{-/-}) cells treated with TZ. Scale bar=10 μ m. Values are (cells with translocated CHMP4B)/(total cell).

(F) Persistence of hCHMP4B-mCherry and hMLKL^(1–140)-2Fv-Venus in digitonin-treated cells, following MLKL activation. Dox-inducible hMLKL^(1–140)-2Fv-Venus in *mkl1*^{-/-} MEF were silenced with the indicated siRNA and treated as in (B). 100 nM B/B was added (30 min), and cells were treated with digitonin before FACS analysis. MFI for Venus and mCherry were compared with and without B/B. An MFI ratio fold-change of the B/B-treated/control cells of 1 indicates no difference in the persistence of the fluorescent signal.

(G–I) Z-stack confocal microscope images of RIPK3-2Fv-NIH3T3 (upper panel) and hMLKL^{1–181}-2Fv-NIH3T3 (lower panel), transfected with the indicated siRNA (72 h), followed by addition of B/B (100 nM, 30 min). Cells were stained with AnnV-AF488. Scale bar=1 μ m. For the quantification of bubbles (H and I), bubbles 0.5 μ m were counted in Z-stacked confocal images. Each point represents one cell analyzed. (* $p < 0.05$, *** $p < 0.001$, **** $p < 0.0001$, unpaired Student's t-test).

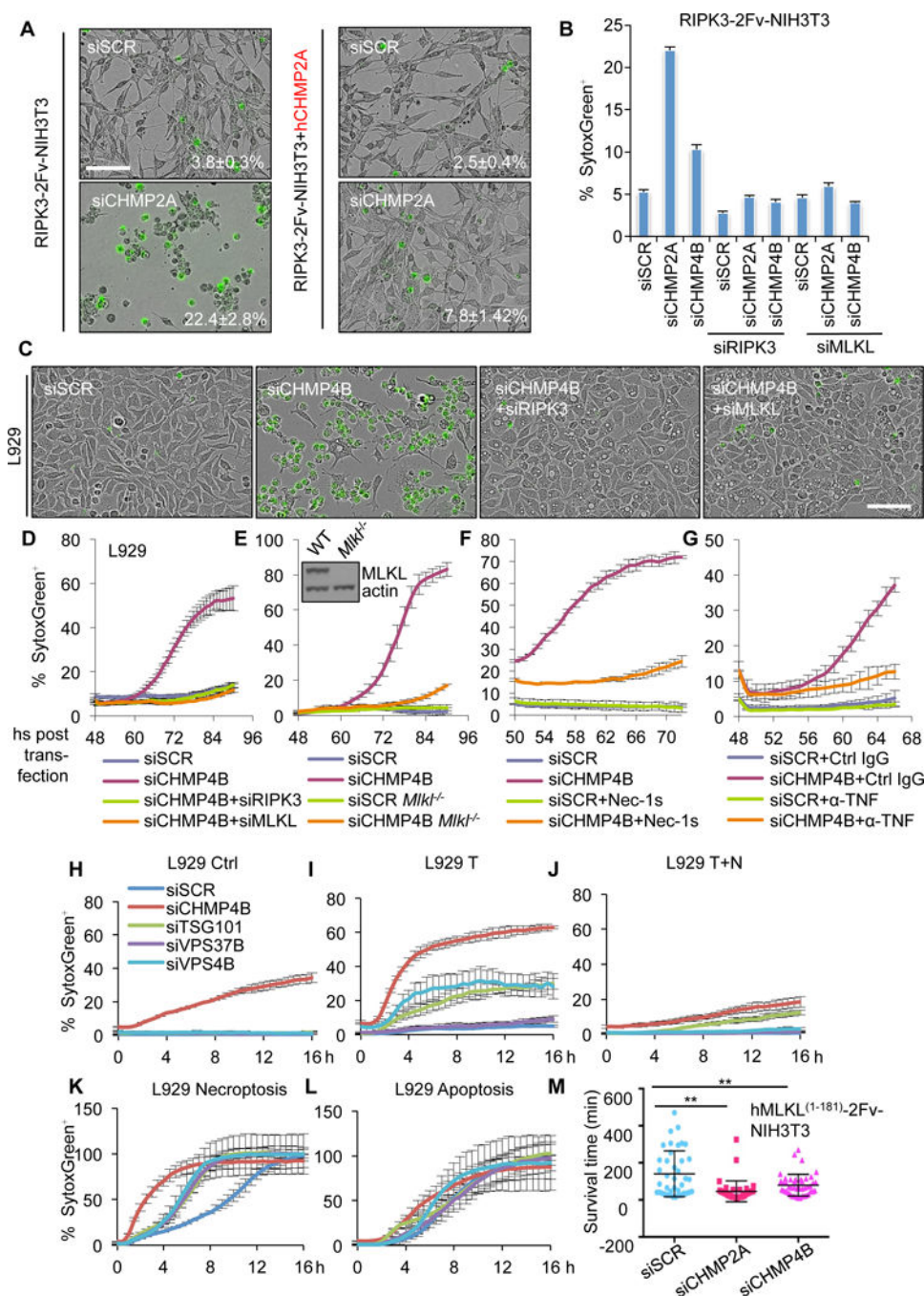


Figure 4. ESCRT-III antagonizes necroptotic cell death

(A) Incucyte images of SytoxGreen stained RIPK3-2Fv-NIH3T3 and hCHMP2A-expressing RIPK3-2Fv-NIH3T3 cells transfected with the indicated siRNA for 72h. Values are the percentage of SytoxGreen⁺ cells (determined by flow cytometry). Scale bar=100 μ m.

(B) Flow cytometric quantification of SytoxGreen⁺ RIPK3-2Fv-NIH3T3 cells transfected with the indicated siRNA for 72 h.

(C–D) Representative Incucyte images at 90 hrs (C) and quantification over time (D) of SytoxGreen stained L929 cells transfected with the indicated siRNA. Scale bar=100 μ m. (E)

Incucyte quantification of SytoxGreen⁺ L929 and L929 *Mkl1*^{-/-} cells transfected with the indicated siRNA. MLKL deletion was confirmed by western blot.

(F) Incucyte quantification of SytoxGreen⁺ L929 cells transfected with the indicated siRNA in the presence or absence of 60 μ M Nec-1s. Nec-1s was added at 50 h post siRNA transfection.

(G) Incucyte quantification of SytoxGreen⁺ L929 cells with indicated siRNA in the presence or either 15 μ g/mL control rat IgG or anti-TNF IgG (α -TNF). Antibodies were added at 48 h post siRNA transfection.

(H–L) Incucyte quantification of SytoxGreen⁺ L929 cells transfected with the indicated siRNA. Cells were treated with control media (H), 20 ng/mL TNF α (I), 20 ng/mL TNF α plus 60 μ M Nec-1s (J), 50 μ M zVAD (K, necroptosis) or 20 ng/mL TNF α , 60 μ M Nec-1s, or 10 μ g/mL Cycloheximide (L, apoptosis). Treatments were added 68h post transfection. (M) Confocal quantification of survival time of GCaMP3-expressing hMLKL¹⁻¹⁸¹-2Fv-NIH3T3 cells treated with 100 nM B/B. Each point indicates one cell. “Survival time” is the time from GCaMP3 fluorescence (Ca⁺⁺ influx) to loss of plasma membrane integrity. (**p < 0.01, unpaired Student’s t-test).

For all Incucyte quantification, data are presented as mean of at least triplicate samples. For all FACS quantification, data are presented as mean of triplicate samples. In all cases, error bars are s.d.

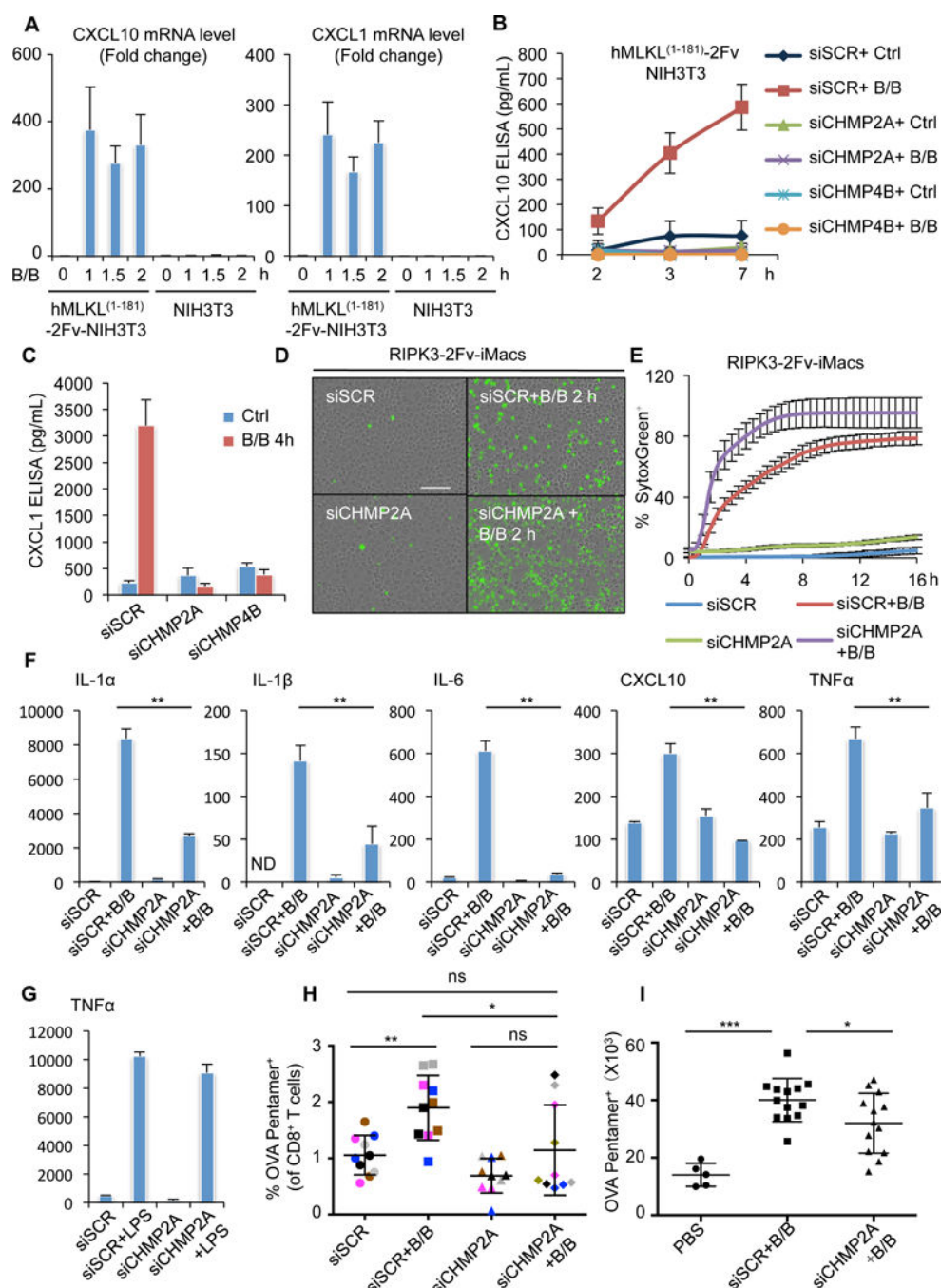


Figure 5. ESCRT-III allows necroptotic cells to signal

(A) qRT-PCR quantification of transcriptional induction of CXCL10 and CXCL1 in hMLKL¹⁻¹⁸¹-2Fv-NIH3T3 cells following the addition of 100 nM B/B addition. Data are mean of triplicate samples \pm s.d.

(B–C) ELISA measurement of CXCL10 (B) and CXCL1 (C) secretion in hMLKL¹⁻¹⁸¹-2Fv-NIH3T3 cells stimulated with 100 nM B/B. Data are mean of at least triplicate samples \pm s.d.

(D–E) Representative Incucyte images (D) and quantification (E) of SytoxGreen⁺ RIPK3-2Fv-iMacs (immortalized macrophages) cells stimulated with 100 nM B/B. Scale bar=100 μ m. For Incucyte quantification (E), data are mean of triplicate samples \pm s.d.

(F) IL-1 α , IL-1 β , IL-6, CXCL10 and TNF α secretion of the cells in (D, 20 h post B/B addition), measured by Luminex. Data are mean of triplicate samples \pm s.d. ND, non-detectable. (pg/mL)

(G) TNF α secretion, measured by ELISA, of the RIPK3-2Fv-iMacs cells stimulated with 5 μ g/mL LPS for 4.5 h. Data are mean of triplicate samples \pm s.d. (pg/mL)

(H–I) ESCRT-III controls the efficiency of induction of T cell cross-priming by necroptotic cells. Each point represents one lymph node (H) or the mean value of two lymph nodes from the same mouse (I). Color indicates lymph nodes from the same mice (H). Transferrin receptor ovalbumin fusion protein (TfR-OVA) was either transiently (H) or stably (I) expressed in RIPK3-2Fv-NIH3T3 cells. Cells were treated with the indicated siRNA for 72 hrs, followed by exposure to B/B (100 nM for 25 min) and injected into mice i.d. After 9 days, Pentamer⁺ CD8⁺ T cells were assessed by FACS. (ns—not statistically significant, * $p < 0.05$, ** $p < 0.01$, *** $p < 0.001$, one-way ANOVA with Tukey test).

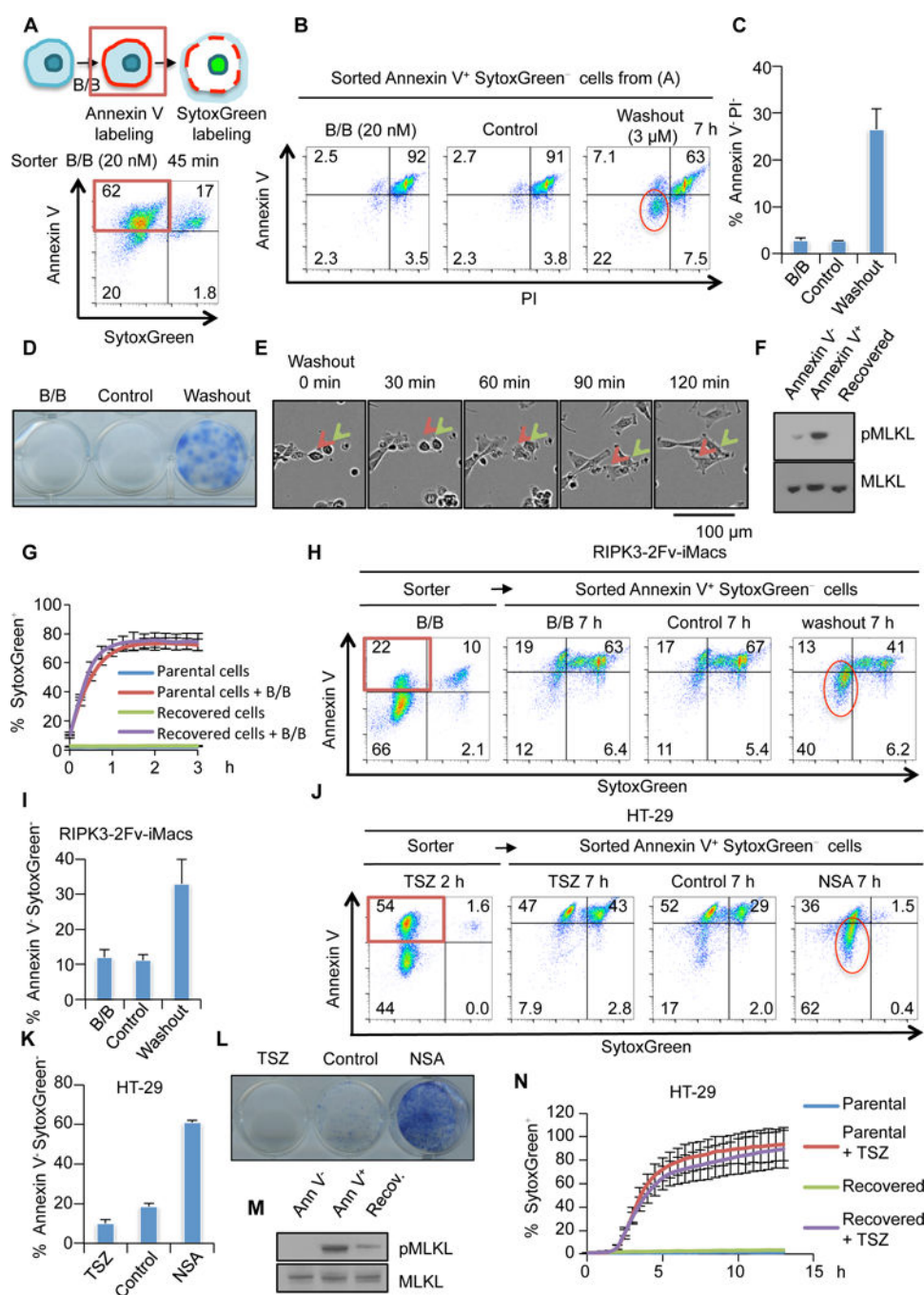


Figure 6. Cells with active MLKL can be resuscitated

(A) Sorting strategy for AnnV⁺ and SytoxGreen⁻ RIPK3-2Fv-NIH3T3 cells. Cells in the red gate were sorted for the following experiments.

(B–C) The sorted cells from (A) were then treated with B/B (20 nM), control media or washout ligand (3 μ M) for 7 h and analyzed by FACS. “Resuscitated” cells are circled in red. Quantification of cell resuscitation is shown in (C).

(D) Clonogenic survival of the cells from (C).

(E) Representative Incucyte imaging of RIPK3-2Fv-NIH3T3 cell resuscitation. Cells were treated with 20 nM B/B for 45 min before the direct addition of 3 μ M washout ligand.

(F) Immunoblotting of phosphorylated MLKL (pMLKL) and total MLKL in cells from (C).

(G) Incucyte quantification of SytoxGreen⁺ parental RIPK3-2Fv-NIH3T3 cells and the recovered RIPK3-2Fv-NIH3T3 cells from (C), after treatment with 100 nM B/B.

(H–I) FACS plots and quantification of cell resuscitation of RIPK3-2Fv-iMacs treated as in (A–C). Cell death was induced by 20 nM B/B for 2 h, followed by cell sorting (red box) and addition of washout agent. Resuscitated cells are circled in red.

(J–K) HT-29 cells were treated with TSZ and AnnV⁺ SytoxGreen[−] (red box) were sorted. Cells were then cultured with 5 μ M NSA. Cell resuscitation was assessed as in (A and B). Quantification is shown in (K).

(L) Clonogenic survival of the cells from (J).

(M) Immunoblotting of phosphorylated MLKL (pMLKL) and total MLKL of the cells from (J).

(N) Incucyte quantification of SytoxGreen⁺ parental HT-29 cells and the recovered HT-29 from (J), following treatment with TSZ.

For all FACS quantification, data are mean of triplicate samples \pm s.d. (ns—not statistically significant, ** $p < 0.01$, unpaired Student's t-test). For all Incucyte quantification, data are mean of at least triplicate samples \pm s.d.

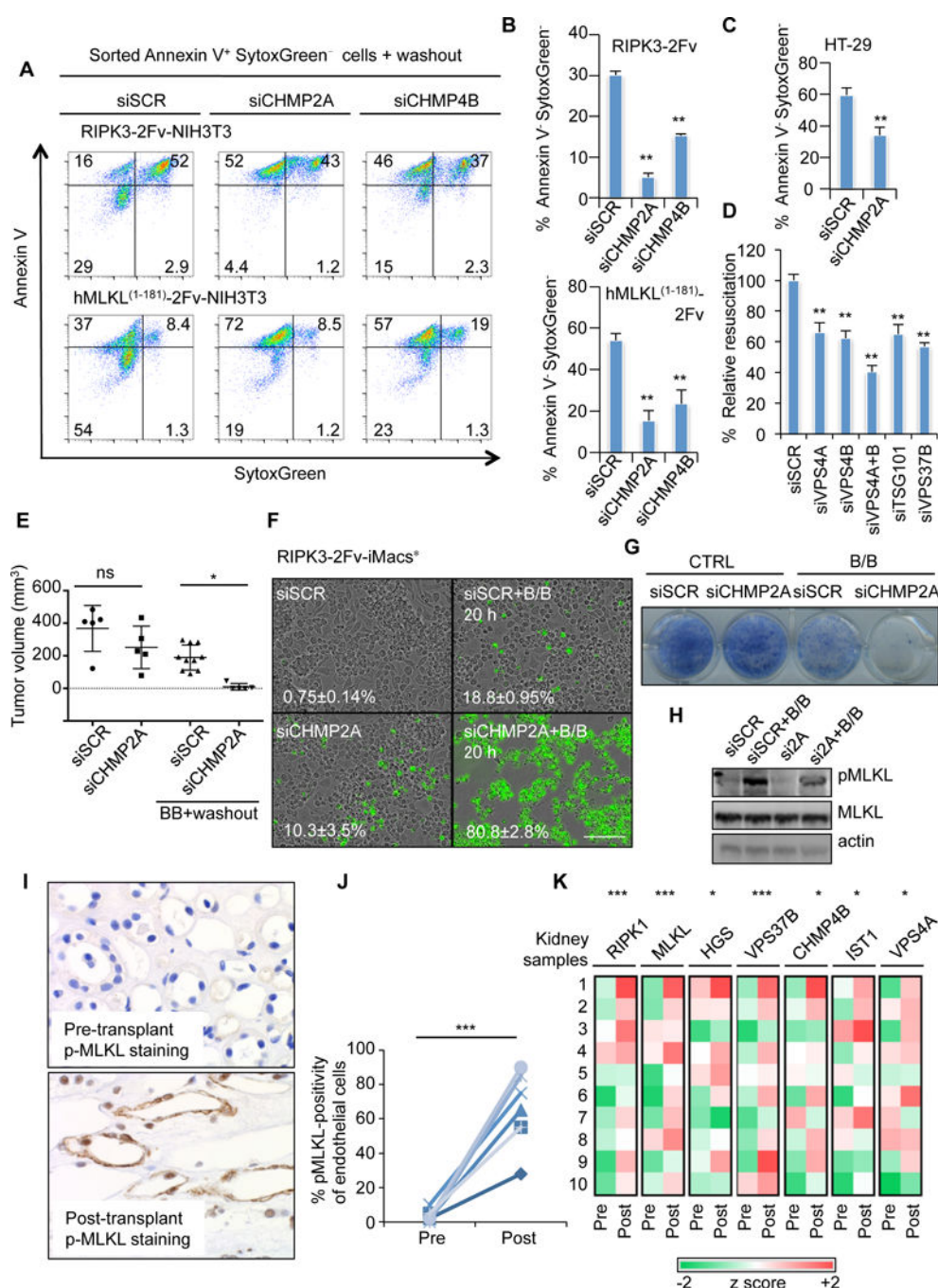


Figure 7. ESCRT machinery preserves cell survival in cells with active MLKL

(A–B) Cells transfected with the indicated siRNA were treated and resuscitated as in Figure 6 (A–C). Shown are representative FACS plots (A) and quantification (B).

(C) HT-29 cells were transfected with the indicated siRNA and resuscitated as in Figure 6 (J). Quantification of resuscitation was assessed by flow cytometry.

(D) The effect of silencing of assorted ESCRT machinery components on the efficiency of RIPK3-2Fv-NIH3T3 cell resuscitation.

(E) Xenograft tumor growth of RIPK3-2Fv-NIH3T3 cells, treated with the indicated siRNA, followed by B/B and resuscitation. Cells were treated with B/B for 45 min, AnnV⁺ SytoxGreen⁻ cells were sorted, followed by treatment with washout ligand for 45 min *in vitro* before intra-dermal injection. Tumor volume was assessed after 2 weeks. (ns—not statistically significant, * $p < 0.05$, one-way ANOVA with Tukey test).

(F–G) A clone of RIPK3-2Fv-iMacs cells (noted as RIPK3-2Fv-iMacs*) was stimulated with 100 nM B/B for 20 h. Shown in (F) are representative Incucyte images and the percentage of SytoxGreen⁺ cells. Data are mean of triplicate samples \pm s.d. Clonogenic survival of the cells from (F) is shown in (G).

(H) Phospho-MLKL in B/B (2.5 h)-treated RIPK3-2Fv-iMacs* cells, determined by western blot.

(I–K) Sections of matched pairs of pre-transplant and post-transplant human renal biopsies were stained with human pMLKL (S358). Note that in the post-transplant section, the endothelial cells with pMLKL staining had an intact plasma membrane. Quantification is shown in (J) (n=7) (** $p < 0.001$, paired Student's t-test). (K) RNA-seq data from the matched pairs of pre-transplant and post-transplant biopsies in (I). (n=10) (* $p < 0.05$, *** $p < 0.001$, paired Student's t-test).

For all FACS quantification, data are mean of triplicate samples \pm s.d. (ns—not statistically significant, ** $p < 0.01$, unpaired Student's t-test).

REAGENT or RESOURCE	SOURCE	IDENTIFIER
Antibodies		
Actin	Santa Cruz	Cat# sc-1616
ALIX (3A9)	Cell Signaling Technology	Cat# 2171S
CHMP2B	Abcam	Cat# ab33174
CHMP4B	Abcam	Cat# ab105767
FLAG	Sigma	Cat# A8592
HA	Sigma	Cat# H6908
I κ B α	Santa Cruz	Cat# C-21
MLKL (human)	Sigma	Cat# M6697
MLKL (murine)	Agent	Cat# AP14272b
pMLKL (human)	Abcam	Cat# ab187091
pMLKL (murine)	Abcam	Cat# ab196436
RIPK3	Novus	Cat# NBP1-77299
TNF	BioXCell	Cat# Clone XT3.11
TSG101 (4A10)	abcam	Cat# ab83
CD8a-APC	eBioscience	Cat# 17-0081-83
Biological Samples		
Human living donor kidney samples	This study	Karolinska University Hospital, Stockholm, Sweden.
Chemicals, Peptides, and Recombinant Proteins		
Annexin V-Alexa Fluor-488	Life technology	Cat# A13201
Annexin V-Alexa Fluor-647	Life technology	Cat# A23024
Sytox Green	Life technology	Cat# S7020
Annexin V-PE	eBioscience	Cat# BMS106PE/100
Annexin V-FITC	eBioscience	Cat# BMS106FI/100
Annexin V-APC	eBioscience	Cat# BMS106APC/100
MFG-E8-FITC	Haematologic Technologies	Cat# BLAC-FITC
DiI stain	Life technology	Cat# D282
10 kD Dextran-NH ₂ -Alexa Fluor 647	Life technology	Cat# D22914
Lcl-161	Chemietek	Cat# 1005342-46-0
7-Cl-O-Nec-1 (Nec-1s)	calbiochem	Cat# 504297
Cycloheximide	Sigma	Cat# C-7698
Q-VD-OPh (qVD)	Apexbio	Cat# A8165
Necrosulfonamide	calbiochem	Cat# 480073
zVAD-fmk	Apexbio	Cat# A1902
BAPTA-AM	Tocris	Cat# 2787
Bafilomycin A1	Sigma	Cat# B1793
LPS	Sigma	Cat# L4391
Digitonin	Sigma	Cat# D141

REAGENT or RESOURCE	SOURCE	IDENTIFIER
B/B dimerizer	Clontech	Cat# 635059
Washout ligand	Clontech	Cat# 635088
PE labeled H-2Kb/OVA (SIINFEKL) Pro5 MHC Pentamer	Proimmune	Cat# F093-2A
Lipofectamine LTX Reagent with PLUS™ Reagent	Invitrogen	Cat# 15338100
INTERFERin	Polyplus-transfection	Cat# 409-10
Lipofectamine RNAiMAX	Invitrogen	Cat# 13778075
Fibronectin	EMD Millipore	Cat# FC010
mTNF	Peprtech	Cat# 315-01A
hTNF	Peprtech	Cat# 300-01A
mIFN-β	EMD Millipore	Cat# IF011
Critical Commercial Assays		
CXCL10 ELISA	eBioscience	Cat# BMS6018
CXCL1 ELISA	R & D	Cat# MKC00B
Milliplex MAP kit	Millipore	Cat# MCYTOMAG-70K-PMX
SYBR Green PCR Master Mix	Applied Biosystem	Cat# 1609503
TNF ELISA	R & D	Cat# MTA00B
RNAzol® RT	Molecular Research Center	Cat# RN 190
QIAcube	Qiagen	Cat# 9001292
TruSeq Stranded mRNA Library Prep Kit	Illumina	Cat# RS-122-2103
RNeasy Mini Kit	Qiagen	Cat# 74106
Deposited Data		
mRNA array data for B/B induced hMLKL ¹⁻¹⁸¹ -2Fv-NIH3T3 cells	This study	GEO: GSE85660
Human kidney biopsies RNA-seq	This study	https://www.obvibas.e.com/#token/cHluy8Hv4Cdb/r/hka6j0CQmzwp
Mouse kidney biopsies microarray	Liu et al., 2014	GEO: GSE52004
Experimental Models: Cell Lines		
RIPK3-2Fv-NIH3T3	Yatim et al., 2015	N/A
RIPK3-2Fv-NIH3T3 ^{MIK1-/-}	This study	N/A
RIPK3-2Fv-NIH3T3+ ovalbumin	Yatim et al., 2015	Gift from Dr. Andrew Oberst Lab
Flag-MLKL-RIPK3-2Fv-NIH3T3 ^{MIK1-/-}	This study	N/A
hMLKL ¹⁻¹⁸¹ -2Fv-NIH3T3	This study	N/A
MEF ^{MIK1-/-}	Quarato et al., 2016	N/A
hMLKL ¹⁻¹⁴⁰ -2Fv-Venus-MEF ^{MIK1-/-}	Quarato et al., 2016	N/A
hMLKL ¹⁻¹⁸¹ -2Fv-MEF ^{MIK1-/-}	This study	N/A
hMLKL ^{FL} -2Fv-MEF ^{MIK1-/-}	This study	N/A
L929 ^{MIK1-/-}	This study	N/A
HT-29 ^{MIK1-/-}	This study	N/A

REAGENT or RESOURCE	SOURCE	IDENTIFIER
MEFs: <i>Tmem16f</i> ^{+/+} , <i>Tmem16f</i> ^{+/−} and <i>Tmem16f</i> ^{−/−}	This study	N/A
Experimental Models: Organisms/Strains		
Mouse: C57BL/6J	Jackson Laboratory	Stock #:000664
Mouse: <i>Rag-1</i> ^{−/−}	Jackson Laboratory	Stock #:002216
Mouse: <i>Tmem16f</i> ^{−/−}	Gift from Dr. Florian Winau (Boston Children's Hospital)	N/A
Oligonucleotides		
siRNA See Table S3	This study	N/A
Primers for qPCR See Table S3	This study	N/A
Recombinant DNA		
"humanized" mouse MLKL	This paper	N/A
Flag-mouse MLKL	This paper	N/A
TfR-OVA	Gift from Dr. Helen Beere (St. Jude Children's Research Hospital).	N/A
GFP-CHMP4B	Gift from Dr. Paul Bieniasz (Rockefeller University)	N/A
hCHMP4B-mCherry	Gift from Dr. Jennifer Lippincott-Schwartz (Janelia Research Campus)	N/A
hMLKL ¹⁻¹⁸¹ -2Fv	This study	N/A
hMLKL ^{FL} -2Fv	This study	N/A
GCaMP3	This study	N/A
pSpCas9(BB)-2A-GFP (PX458)	Addgene	#48138
Software and Algorithms		
IncuCyte FLR	Essen Bioscience	http://www.essenbioscience.com/en/products/software/
Zoom imaging system	Essen Bioscience	http://www.essenbioscience.com/en/products/software/
xPONENT	Luminex Corporation	https://www.luminexcorp.com/clinical/instruments/xponent/
FlowJo	FlowJo LLC	https://www.flowjo.com/
3i Slidebook 6	3i	https://www.intelligent-imaging.com/slidebook
AxioVision Rel. 4.5	Zeiss	https://www.zeiss.com/microscopy/int/downloads/axiovision-downloads.html
HiSeq Control Software 2.2.58	Illumina	https://support.illumina.com/sequencing/sequencing_instruments/hiseq_2500/downloads.html